General Disclaimer

One or more of the Following Statements may affect this Document

- This document has been reproduced from the best copy furnished by the organizational source. It is being released in the interest of making available as much information as possible.

- This document may contain data, which exceeds the sheet parameters. It was furnished in this condition by the organizational source and is the best copy available.

- This document may contain tone-on-tone or color graphs, charts and/or pictures, which have been reproduced in black and white.

- This document is paginated as submitted by the original source.

- Portions of this document are not fully legible due to the historical nature of some of the material. However, it is the best reproduction available from the original submission.

Produced by the NASA Center for Aerospace Information (CASI)

NASA TECHNICAL MEMORANDUM

NASA TM X-73361

(NASA-TM-X-73361) NUMERICAL SOLUTIONS OF NAVIER-STOKES EQUATIONS FOR THE STRUCTURE OF A TRAILING VORTEX (NASA) 66 p HC A04/MF A01 CSCL 01A

N77-16993

Unclas

G3/02 15601

NUMERICAL SOLUTIONS OF NAVIER-STOKES EQUATIONS FOR THE STRUCTURE OF A TRAILING VORTEX

By A. C. Jain
Systems Dynamics Laboratory

MAR 1977
RECEIVED
NASA STI FACILITY
INPUT BRANCH

January 1977

NASA

George C. Marshall Space Flight Center
Marshall Space Flight Center, Alabama

TECHNICAL REPORT STANDARD TITLE PAGE

1. REPORT NO.	2. GOVERNMENT ACCESSION NO.	3. RECIPIENT'S CATALOG NO.
NASA TM X-73361		

4. TITLE AND SUBTITLE	5. REPORT DATE
Numerical Solutions of Navier-Stokes Equations for the Structure of a Trailing Vortex	January 1977
	6. PERFORMING ORGANIZATION CODE
7. AUTHOR(S) A. C. Jain*	8. PERFORMING ORGANIZATION REPORT #
9. PERFORMING ORGANIZATION NAME AND ADDRESS	10. WORK UNIT NO.
George C. Marshall Space Flight Center Marshall Space Flight Center, Alabama 35812	11. CONTRACT OR GRANT NO.
12. SPONSORING AGENCY NAME AND ADDRESS	13. TYPE OF REPORT & PERIOD COVERED
National Aeronautics and Space Administration Washington, D. C. 20546	Technical Memorandum
	14. SPONSORING AGENCY CODE

15. SUPPLEMENTARY NOTES

Prepared by Systems Dynamics Laboratory, Science and Engineering
*On leave from Indian Institute of Technology, Kanpur, India.

16. ABSTRACT

An attempt is made to understand the structure and decay of a trailing vortex through the numerical solutions of the full Navier-Stokes equations. Unsteady forms of the governing equations are recast in terms of circulation, vorticity, and stream function as dependent variables, and a second upwind finite difference scheme is used to integrate them with prescribed initial and boundary conditions. A discussion of the boundary conditions at the outer edge and at the outflow section of the trailing vortex is included. Different models of the flow are postulated, and solutions are obtained describing the development of the flow as integration proceeds in time. A parametric study is undertaken with a view to understand the various phenomena that may possibly occur in the trailing vortex. Using the Hoffman and Joubert law of circulation at the inflow section, the results of the present investigation are compared with the experimental data of Chigier and Corsiglia on a Convair 990 wing model and a rectangular wing. With an exponentially decaying law of circulation at the inflow section and an adverse pressure gradient at the outer edge of the trailing vortex, solutions depict vortex bursting through the sudden expansion of the core and/or through the stagnation and consequent reversal of the flow on the axis. It is found that this bursting takes place at lower values of the swirl ratio as the Reynolds number increases.

17. KEY WORDS	18. DISTRIBUTION STATEMENT
	Unclassified — Unlimited

19. SECURITY CLASSIF. (of this report)	20. SECURITY CLASSIF. (of this page)	21. NO. OF PAGES	22. PRICE
Unclassified	Unclassified	67	NTIS

MSFC - Form 3292 (Rev December 1972)

For sale by National Technical Information Service, Springfield, Virginia 22151

ACKNOWLEDGMENT

The author is greatly indebted to Mr. Werner K. Dahm, Chief, Aerophysics Division, Marshall Space Flight Center, for introducing him to this interesting problem. He gratefully acknowledges the benefit of his valuable advice and many fruitful discussions.

Thanks are also due to Mr. Al Gessow of National Aeronautics and Space Administration Headquarters and to Mr. Milton Huffakar of Marshall Space Flight Center for their keen interest and kind encouragement. The research was conducted while the author was pursuing a NAS/NRC Senior Research Associateship at Marshall Space Flight Center, Alabama, from August 1972 until December 1974. The manuscript was written after joining the faculty of I. I. T., Kanpur, India.

TABLE OF CONTENTS

		Page
SUMMARY		1
I.	INTRODUCTION	2
II.	GOVERNING EQUATIONS OF MOTION	4
III.	DESCRIPTION OF NUMERICAL METHOD	10
IV.	DISCUSSION OF NUMERICAL BOUNDARY CONDITIONS AT THE OUTFLOW SECTION AND AT THE OUTER EDGE OF THE TRAILING VORTEX	15
V.	DISCUSSION OF RESULTS	17
VI.	CONCLUDING REMARKS	25
REFERENCES		57

LIST OF ILLUSTRATIONS

Figure	Title	Page
1.	Coordinate system	25
2.	$v_Z(Z, 0)$, $(v_\phi)_{max}$ and r_{core} versus Z with different mesh sizes	26
3.	$v_Z(Z, 0)$ versus Z with different outer edge conditions	27
4.	$(v_\phi)_{max}$ versus Z with different outer edge conditions	28
5.	$v_Z(Z, 0)$ versus Z for different $v_Z(Z_1, 0)$	29
6.	$(v_\phi)_{max}$ and core growth, r_{core}, versus Z for different $v_Z(Z_1, 0)$	30
7.	$v_Z(Z, 0)$, $(v_\phi)_{max}$ and γ_{core} versus Z for different values of core radius at inflow section	31
8.	v_ϕ versus radial distance 'r' at Z = 5.0 for different (r_1)	32
9.	$v_Z(Z, 0)$, $(v_\phi)_{max}$ and core growth, r_{core}, versus 'Z' for different values of 'α'	33
10.	$v_Z(Z, 0)$ versus Z for different values of Reynolds number	34
11.	$(v_\phi)_{max}$ versus Z for different values of Reynolds number	35
12.	$v_Z(Z, 0)$, $(v_\phi)_{max}$ and, r_{core}, versus 'Z' for different values of swirl ratio	36

LIST OF ILLUSTRATIONS (Continued)

Figure	Title	Page
13.	$(v_\phi / V_1)_{max}$, $v_Z(Z, 0)$ and core growth, r_{core}, versus 'Z' for different values of swirl ratio	37
14.	Comparison of the present results of $v_Z(Z, 0)$, $(v_\phi / V_1)_{max}$ and, r_{core}, versus 'Z' with corresponding experimental data of Reference 12	38
15.	v_ϕ versus r at various sections in downstream direction	39
16.	Comparison of the present results for $v_Z(Z, 0)$ versus Z with the experimental data of Reference 12	40
17.	Comparison of the present results for $(v_\phi / V_1)_{max}$ versus Z with the experimental data of Reference 12	40
18.	Comparison of present results for core growth r_{core} versus Z with the experimental data of Reference 12	41
19.	Comparison of the present results for v_Z versus r with the experimental data of Reference 12	41
20.	Comparison of the present results for (v_ϕ / U_∞) versus r with the experimental data of Reference 12	42
21.	Comparison of the present results for (v_Z / U_∞) versus 'r' with the experimental data of Reference 12	43
22.	Comparison of the present results for v_ϕ / U_∞ versus r with the experimental data of Reference 12	44

LIST OF ILLUSTRATIONS (Concluded)

Figure	Title	Page
23.	$v_Z(Z, 0)$ versus Z for different prescribed axial velocity at the inflow section and at the outer edge of the trailing vortex	45
24.	$v_Z(Z, 0)$ versus Z for different values of Reynolds number	46
25.	$v_Z'(Z, 0)$ versus Z for different values of the swirl ratio	47
26.	r_{core} versus Z for different values of swirl ratio	48
27.	$(v_\phi / V_1)_{max}$ versus Z for different values of swirl ratio	49
28.	v_ϕ / V_1 versus r at different sections in the downstream direction	50
29.	Streamline pattern for swirl ratio = 0.6, stream function values those shown $\times 10^{-2}$	51
30.	Streamline pattern for swirl ratio = 0.65, stream function values those shown $\times 10^{-2}$	52
31.	Streamline pattern for swirl ratio = 0.7, stream function values those shown $\times 10^{-2}$	53
32.	Streamline pattern for swirl ratio = 0.8, stream function values those shown $\times 10^{-2}$	54

DEFINITION OF SYMBOLS

Symbol	Definition
C	mid-chord length of wing
r	radial coordinate
r_1	local vortex core radius; $r_1 = r_{v_{\varphi\,max}}$
Re	Reynolds number; $Re = U_\infty C/\nu$
t	time
U_∞	ambient velocity
v_r, v_φ, v_Z	velocity components in direction of the 3 coordinates
V_1	maximum of v_φ at inflow section
V_1/U_∞	swirl ratio
Z	axial coordinate
Z_1	axial coordinate of inflow section
Z_2	axial coordinate of outflow section
Γ	circulation; $\Gamma = rv_\varphi$
Δ	axial velocity defect at center of inflow section ($Z = Z_1$, $r = 0$)

$$\Delta = \frac{U_\infty - (v_Z')_{r=0}}{U_\infty} = 1 - v_Z$$

DEFINITION OF SYMBOLS (Concluded)

Symbol	Definition
η	vorticity; $\eta = \frac{\partial v_r}{\partial Z} - \frac{\partial v_Z}{\partial r}$
ν	kinematic viscosity
φ	azimuthal coordinate
ψ	stream function

TECHNICAL MEMORANDUM X-73361

NUMERICAL SOLUTIONS OF NAVIER-STOKES EQUATIONS FOR THE STRUCTURE OF A TRAILING VORTEX

SUMMARY

This report describes the structure and decay of a trailing vortex through the numerical solutions of the full, unsteady Navier-Stokes equations. The governing equations are recast in terms of circulation, vorticity, and stream function as dependent variables, and a second upwind finite difference scheme is used to integrate them with prescribed initial and boundary conditions using Univac 1108 and IBM 360 computers. The time-dependent numerical solutions are carried out within a cylindrical volume that is coaxial with the vortex with prescribed boundary conditions on the upstream face, on the axis of symmetry, and on the cylindrical outer boundary.

Different models of the flow are postulated, and solutions are obtained describing the development of the flow as integration proceeds in time. A parametric study is undertaken with a view to understand the various phenomena that may possibly occur in the trailing vortex.

Using the Hoffman and Joubert law of circulation at the inflow section, results obtained with the present method are compared with the experimental data of Chigier and Corsiglia on a Convair 990 wing model and a rectangular wing. The calculated results compare reasonably well with the experimental results on axial and tangential velocity distributions and their decay, axial velocity variation along the axis, and core growth. The flow with different values of the governing parameters is computed. This parametric study greatly increases our understanding of the manner in which the flow dissipates downstream.

Particular difficulty is experienced in getting convergent solutions with high values of the swirl parameter. With an exponentially decaying circulation distribution and uniform axial flow at the inflow section and at the outer edge of the trailing vortex, we get convergent solutions, but the computer time increases

excessively as the swirl ratio increases. Also, it is found that the trailing vortices persist to long distances downstream before decay. Due to the slow development and decay of the vortex core in streamwise direction, vortex bursting could not be obtained within the limits of available computer time when "uniform" boundary conditions were used.

To force bursting within a reasonable computer time, an adverse pressure gradient was imposed on the trailing vortex in the ambient fluid. A bursting phenomenon was obtained under this condition. A sudden jump in the core radius occurred even before the reversal of the flow on the axis. For a given Reynolds number, slight changes in the swirl ratio exercised a large influence on the bursting bubble. The flow downstream of the bursting rotated like a solid body. There is much need to carry out more numerical experiments to understand better this bursting phenomenon as a function of the governing parameters and interpret the sudden increase in the core growth in the light of available theories.

I. INTRODUCTION

A basic understanding of the various phenomena occurring in a trailing vortex is essential to assess the hazards to an encountering aircraft and to predict transport and dissipation rates. Such an understanding is also required for the safe operation of the aircraft in the terminal areas and for the development of techniques for increasing the dissipation rates. In this investigation, an attempt is made to develop an exact procedure of predicting the structure of a trailing vortex under various ambient and prescribed conditions.

An early attempt to solve the problem was made by Newman [1], who linearized the Navier-Stokes equations and neglected the pressure gradient term. He obtained analytical expressions for the circulation distribution and for the radial and axial velocities. The main contribution of Newman's work is the analytical derivation of the expressions depicting the exponential decay of circulation and axial and radial velocity distributions. Several investigators have succeeded in matching experimental data with the tangential velocity profile of Newman, using different models of the eddy viscosity. Hall [2,3], Kopecky and Torrance [4], and Bossel [5] used these analytical expressions to provide initial conditions for the computation of the flow further downstream. Later,

Batchelor [6] obtained an analytical solution of the linearized equations with the pressure gradient term. He showed that far downstream, the contribution from the logarithmic term becomes important.

Hall [2] simplified the Navier-Stokes equations by quasi-cylindrical approximation and integrated numerically the resulting parabolic nonlinear equations. At a certain point in the downstream direction, he found large gradients in the flow variables which prohibit the computations from proceeding further. This indicates the failure of the quasi-cylindrical approximation. Hall [3] interpreted this failure as an indication of the onset of a breakdown similar to the failure of the boundary layer equations near the separation point. This analogy may not be strictly valid because the failure of the quasi-cylindrical approximation occurs when the axial velocity is much greater than zero.

Bossel [5] and Mager [7] solved the governing equations with quasi-cylindrical approximations by the approximate methods of representing the circulation and axial velocity profiles by polynomials. Bossel [5] found, in his solution, an infinite number of discrete singularities whose corresponding critical swirl values depend on velocity and circulation profile shapes. Mager [7] developed a momentum integral method for the core of the trailing vortex and used third and fourth degree polynomials to represent the axial and the swirl velocity distributions, respectively. He also found that for certain values of the velocity ratio and swirl ratio, large gradients in the flow cause the failure of the quasi-cylindrical approximation. He indicated the onset of bursting similar to the one predicted by Hall [3]. He further obtained results on either side of the singularity at breakdown. Sarpkaya [8] obtained results of vortex breakdown under adverse pressure gradients and correlated his experimental data with the theoretical predictions of Mager [7]. It may be pointed out here that Mager's [7] results seem to depend critically on the degree of the profiles chosen. There is a need to investigate the flow with other forms of profiles, particularly the exponential ones.

Kuhn and Nielson [9] developed basic equations on considerations of linear and angular momentum of the vortex and total pressure variation along the axis. Using the Hoffman and Joubert [10] law of circulation distribution at the inflow section, Kuhn and Nielson computed the flow downstream for gross quantities such as the decay of the maximum tangential velocity, the core growth, and the axial velocity distribution on the axis. Comparison of their theoretical predictions with the experimental data of Chigier and Corsiglia [11] seems to be reasonably good.

A number of experiments in actual flight, water tank, smoke chamber, and wind tunnels have been conducted to understand the structure and decay of trailing vortices [11-14]. None of these, so far, gives reliable quantitative or qualitative information concerning the structure, transport, and dissipation of the trailing vortices.

So far, theoretical work to investigate the structure of the flow in the trailing vortex has been done within the framework of a quasi-cylindrical approximation of the Navier-Stokes equations. This analysis is essentially valid in the core region and ignores mutual interaction between viscous and inviscid flow. As such, it can not predict breakdown phenomena with reasonable accuracy.

In this investigation, numerical solutions of the full Navier-Stokes equations are used to describe the structure of the flow in a trailing vortex and its decay or possible bursting. An unsteady form of the Navier-Stokes equations is derived in terms of circulation, vorticity, and stream function as dependent variables. With prescribed conditions at the inflow section on the axis and at the outer edge of a trailing vortex, the governing equations are integrated by the second upwind finite difference numerical scheme on Univac 1108 and IBM 360 computers. The flow develops smoothly in time from the initial conditions to an asymptotic steady state. The flow is essentially laminar. Turbulence is introduced in a simplified way through the concept of eddy viscosity. A fully developed trailing vortex is simulated by a swirling flow coupled with an axial flow. The problem essentially is to prescribe conditions at the inflow section, either from experimental data or from some other theoretical considerations, and to compute the flow downstream. A parametric study of the structure of the flow in the trailing vortex is made and the theoretical predictions are compared with the available experimental data .

II. GOVERNING EQUATIONS OF MOTION

A sketch of the coordinate system and the region of integration is shown in Figure 1. The Navier-Stokes equations for an unsteady axisymmetric flow in nondimensional variables take the following form:

$$\frac{\partial \Gamma}{\partial t} + \frac{\partial}{\partial Z}(v_Z \Gamma) + \frac{1}{r}\frac{\partial}{\partial r}(r v_r \Gamma) = \frac{1}{Re}\left[\frac{\partial^2 \Gamma}{\partial Z^2} + r\frac{\partial}{\partial r}\left(\frac{1}{r}\frac{\partial \Gamma}{\partial r}\right)\right] \quad (1)$$

$$\frac{\partial \eta}{\partial t} + \frac{\partial}{\partial Z}(v_Z \eta) + \frac{\partial}{\partial r}(v_r \eta) = 2\left(\frac{V_1}{U_\infty}\right)^2 \cdot \frac{\Gamma}{r^3} \cdot \frac{\partial \Gamma}{\partial Z}$$

$$+ \frac{1}{Re}\left\{\frac{\partial^2 \eta}{\partial Z^2} + \frac{\partial}{\partial r}\left[\frac{1}{r}\frac{\partial}{\partial r}(r\eta)\right]\right\} \tag{2}$$

$$\frac{1}{r}\frac{\partial^2 \psi}{\partial Z^2} + \frac{\partial}{\partial r}\left(\frac{1}{r}\frac{\partial \psi}{\partial r}\right) = -\eta \quad , \tag{3}$$

where r, φ, Z are the radial, azimuthal and axial coordinates, and v_r, v_φ, v_Z are the components of velocity in the corresponding directions.

The variables are made dimensionless as follows:

$$t = \frac{U_\infty}{C} t' \quad , \quad Z = \frac{Z'}{C} \quad , \quad r = \frac{r'}{C}$$

$$v_r = \frac{v'_r}{C} \quad , \quad v_\varphi = \frac{v'_\varphi}{V_1} \quad , \quad v_Z = \frac{v'_Z}{U_\infty}$$

$$\Gamma = \frac{\Gamma'}{CV_1} \quad , \quad \eta = \frac{C}{U_\infty}\eta' \quad , \quad \psi = \frac{\psi'}{C^2 U_\infty} \quad .$$

Here, a prime indicates a dimensional variable.

<u>Boundary and Initial Conditions</u>

$r = 0 \quad , \quad Z \geq Z_1 \quad : \quad \Gamma = \eta = \psi = 0$

$r > 0 \quad , \quad Z = Z_1 \quad : \quad \Gamma \quad , \quad \eta$ and ψ to be prescribed (see Conditions I and II).

$$r \to \infty \quad , \quad Z \geq Z_1 \quad : \quad \Gamma \to \Gamma_0 \quad , \quad \eta \to 0 \quad , \quad \psi \to \psi_0 \tag{4}$$

where Γ_0 and ψ_0 are the asymptotic values of Γ and ψ (see Section IV)

$r \geq 0$, $Z = Z_2$: Numerical boundary conditions discussed in Section IV.

Here, $Z = Z_1$ and $Z = Z_2$ represent the inflow and outflow sections of the region under consideration.

At $Z = Z_1$, the following two sets of conditions are imposed:

Condition I

(1) Hoffman and Joubert's law [9,10] describes the circulation distribution. In our nondimensional variables, it can be written as

$$\Gamma = 1.47 \frac{r^2}{r_1} \quad , \quad r \leq r_i \tag{5}$$

where r_1 is the radius of the core

$$\Gamma = r_1 \left[1 + 0.928 \ln \left(\frac{r}{r_1} \right) \right] \quad , \quad r_i < r \leq r_j \tag{6}$$

$$\Gamma = r_1 \left[\frac{K_0}{K_1} - 4.43 \, e^{-4.8 \frac{r}{r_0}} \right] \quad , \quad r > r_j \quad . \tag{7}$$

Here

$$K_1 = r_1 V_1$$

$$K_0 = r_0 V_0$$

where r_0, V_0 are the asymptotic values of the radius and the tangential velocity.

$$\frac{K_0}{K_1} = 0.76 - 0.928 \ln\left(\frac{r_1}{r_0}\right) \tag{8}$$

and

$$2\pi K_0 = \frac{1}{4} U_\infty C_L \frac{S}{R}$$

where

S = wing area

R = half of vortex pair separation distance at the inflow section

C_L = lift coefficient.

From the continuity of vorticity and circulation considerations [9],

$$r_i = 0.5625\, r_1 \tag{9a}$$

$$r_j = 0.515\, r_0 \quad . \tag{9b}$$

Here, we need to know r_1 from experimental data.

(2) The axial velocity is represented by

$$v_Z = 1 - \Delta[1 - 6\rho^2 + 8\rho^3 - 3\rho^4] \quad , \tag{10}$$

where

$\rho = r/r_2$, r_2 being the distance from the axis at which the axial velocity is equal to the ambient velocity (let $r_2 = \alpha r_1$ where α is a constant).

$$\Delta = \frac{U_\infty - (v_Z')_{r=0}}{U_\infty} = 1 - v_Z \quad .$$

The axial velocity satisfies the conditions

(a) at $\rho = 0$, $v_Z = 1 - \Delta$

where Δ is positive for a deficit flow and is negative for an excess flow.

$$\frac{\partial v_Z}{\partial \rho} = 0$$

(b) at $\rho = 1$, $\dfrac{\partial v_Z}{\partial \rho} = \dfrac{\partial^2 v_Z}{\partial \rho^2} = 0$

Several numerical experiments were made with a third degree profile dropping the condition $\partial^2 v_Z / \partial \rho^2 = 0$ at $\rho = 1$. It was found that a fourth degree profile gave a smoother merging of the flow with the ambient fluid. It is surmised that higher degree profiles satisfying vanishing gradients of higher order at $\rho = 1$ may give an even smoother and faster merging.

(3) Vorticity $\eta = \dfrac{\partial v_r}{\partial Z} - \dfrac{\partial v_Z}{\partial r} \approx - \dfrac{\partial v_Z}{\partial r}$

$$= -12\Delta\beta^2 r(1 - 2\beta r + \beta^2 r^2) \tag{11}$$

where

$$\beta = \frac{C}{r_2}$$

(4) Stream function

$$\psi = \frac{r^2}{2}\left[1 - \Delta\left(1 - 3\beta^2 r^2 + \frac{16}{5}\beta^3 r^3 - \beta^4 r^4\right)\right] \tag{12}$$

Condition II

Here, we consider an exponentially varying circulation distribution as follows:

$$\Gamma = A(1 - e^{-Br^2}) \tag{13}$$

where A and B are constants. In this investigation, we take A = 0.554, B = 8.0 so that the core radius is approximately (0.4C). For

$$Z = Z_1 \quad , \quad r \geq 0 \quad , \quad v_Z = \Delta(1 - \beta Z) \tag{14}$$

$$\psi = \Delta(1 - \beta Z)\frac{r^2}{2} \tag{15}$$

$$v_r = \Delta\beta\frac{r^2}{2} \tag{16}$$

$$\eta = 0 \cdot 0 \quad . \tag{17}$$

Numerical experiments with various values of Δ and β are carried out. We choose $\Delta = 0.75$ and $\beta = 0.25$ so as to force bursting with reasonable computer time.

III. DESCRIPTION OF NUMERICAL METHOD

A second upwind finite difference scheme was used to integrate equations (1) and (2) for Γ and η, and the method of successive over-relaxation was used for equation (3) for ψ. This method was used previously by a number of investigators [15]. Notable contributions have been made by Torrance [16], Fromm [17], and Donovan [18], who investigated the recirculating fluid motion driven by the combined effects of a moving wall and natural convection in rectangular cavities. Later, Kopecky and Torrance [4] examined the formation of eddies in a rotating stream. Roache and Mueller [19] obtained numerical solutions for the back step flows with and without splitter plates and for flows over square cavities. They discussed the transportive and conservative properties of this method and the importance of numerical boundary conditions to give accurate and convergent solutions of the Navier-Stokes equations. The numerical method used here is essentially the same as that used by Torrance together with other investigators in a number of publications.

The basic method used for equations (1) and (2) at interior grid points is as follows: the radial and axial velocity components are obtained by center differencing of the stream function,

$$(v_r)_{i,j} = -\frac{1}{r}\left(\frac{\partial\psi}{\partial Z}\right)_{i,j} = -\frac{1}{r}\cdot\frac{\psi_{i+1,j} - \psi_{i-1,j}}{2\Delta Z}$$

$$(v_Z)_{i,j} = \frac{1}{r}\left(\frac{\partial\psi}{\partial r}\right)_{i,j} = \frac{1}{r}\cdot\frac{\psi_{i,j+1} - \psi_{i,j-1}}{2\Delta r} \quad . \tag{18}$$

On the axis $r = 0$, using L'Hospital's rule, we get

$$(v_Z)_{i,1} = \frac{2\psi_{i,2}}{(\Delta r)^2} \quad . \tag{19}$$

Here, the subscripts denote the spatial location of a grid point. Circulation and vorticity are then advanced in time:

$$f_{i,j}^{n+1} = f_{i,j}^{n} + (\Delta t) \left\{ -\frac{\partial}{\partial Z}(v_Z f) - \frac{\partial}{\partial r}(v_r f) + P\left[2\left(\frac{V_1}{U_\infty}\right)^2 \frac{\Gamma}{r^3}\frac{\partial \Gamma}{\partial Z}\right] + \frac{P}{Re}\left[\frac{\partial^2 f}{\partial Z^2} + \frac{\partial}{\partial r}\left(\frac{1}{r}\frac{\partial}{\partial r}(rf)\right)\right] + \frac{Q}{Re}\left[\frac{\partial^2 f}{\partial Z^2} + r\frac{\partial}{\partial r}\left(\frac{1}{r}\frac{\partial f}{\partial r}\right)\right]\right\} ,$$

where the variable f represents either the circulation or the vorticity η.

$P = 0$, $Q = 1$ if f is circulation Γ .

$P = 1$, $Q = 0$ if f is vorticity η .

Diffusion and swirl ratio terms in equation (20) are represented by the centered difference formula as follows:

$$\left(\frac{\partial^2 f}{\partial Z^2}\right)_{i,j} = \frac{f_{i+1,j}^{n} - 2f_{i,j}^{n} + f_{i-1,j}^{n}}{(\Delta Z)^2} \tag{21}$$

and

$$\left(\frac{\Gamma}{r^3}\frac{\partial \Gamma}{\partial Z}\right)_{i,j} = \frac{\Gamma_{i,j}^{n+1}}{r^3} \cdot \frac{\Gamma_{i+1,j}^{n+1} - \Gamma_{i-1,j}^{n+1}}{2\Delta Z} . \tag{22}$$

It should be noticed that in equation (22) the latest value of circulation is used.

The advection terms in the second upwind finite difference scheme are treated in a different way. They are approximated by the three-point noncentered finite differences as follows:

$$\frac{\partial}{\partial Z}(v_Z f) = \frac{1}{\Delta Z}\left[(\bar{v}_Z)_{i,j} f_{i,j} - (\bar{v}_Z)_{i-1,j} f_{i-1,j}\right]$$

$$\text{for } (\bar{v}_Z)_{i,j} > 0 \quad \text{and } (\bar{v}_Z)_{i-1,j} > 0 \tag{23a}$$

or

$$= \frac{1}{\Delta Z}\left[(\bar{v}_Z)_{i,j} f_{i+1,j} - (\bar{v}_Z)_{i-1,j} f_{i-1,j}\right]$$

$$\text{for } (\bar{v}_Z)_{i,j} < 0 \quad \text{and } (\bar{v}_Z)_{i-1,j} < 0 \quad , \tag{23b}$$

where

$$(\bar{v}_Z)_{i,j} = \frac{(v_Z)_{i+1,j} + (v_Z)_{i,j}}{2}$$

and

$$(\bar{v}_Z)_{i-1,j} = \frac{(v_Z)_{i,j} + (v_Z)_{i-1,j}}{2} \quad . \tag{24}$$

Similar expressions are used for $\partial(v_r f)/\partial r$. If $(\bar{v}_Z)_{i,j}$ and $(\bar{v}_Z)_{i-1,j}$ are of opposite signs, a mixed expression consisting of the corresponding terms in equation (23a,b) is used for the finite difference approximation. At each iteration, the computer checks the sign of $(\bar{v}_Z)_{i,j}$ and $(\bar{v}_r)_{i,j}$ at each interior grid point and picks up the corresponding formula for the advection terms.

Computations proceed by advancing time (Δt). At each time step, new values of circulation, Γ, and vorticity, η, are obtained in that order according to equation (20). Then, the new stream function ψ is calculated from equation (3) by the method of successive over-relaxation as follows:

$$\psi_{i,j}^{(s+1)} = (1 - \omega_b)\psi_{i,j}^{(s)} + \left\{ \frac{\omega_b}{\frac{2}{(\Delta Z)^2} + \frac{r}{r + \frac{\Delta r}{2}} \cdot \frac{1}{(\Delta r)^2} + \frac{r}{r - \frac{\Delta r}{2}} \cdot \frac{1}{(\Delta r)^2}} \right\}$$

$$\times \left\{ r\eta'_{i,j} + \frac{1}{(\Delta Z)^2}\left(\psi_{i+1,j}^{(s)} + \psi_{i-1,j}^{(s+1)}\right) \right.$$

$$\left. + \frac{r}{r + \frac{\Delta r}{2}} \cdot \frac{1}{(\Delta r)^2} \cdot \psi_{i,j+1}^{(s)} + \frac{r}{r - \frac{\Delta r}{2}} \cdot \frac{1}{(\Delta r)^2} \cdot \psi_{i,j-1}^{(s+1)} \right\} . \tag{25}$$

Here, $\psi_{i,j}^{(s)}$ denotes the stream function at the grid point (i,j) after '$\underline{s}$' iterations. The optimum relaxation factor $\omega_b = 1.7$ is found adequate for good convergence for the given system of grid points. We notice that the most recent values of η and ψ are used in calculating the new ψ field. At each time step, equation (25) for ψ is iterated until the maximum difference at the grid points between successive values of ψ at each time step is $\leq 10^{-4}$. Velocity components are then calculated according to equation (18), and the new values of Γ and η are calculated at the next time step.

To avoid computational instability, the critical time step at each grid point is given by

$$(\Delta t)_{crit} = \left[\frac{(\bar{v}_Z)_{i,j}}{\Delta Z} + \left(1 + \frac{\Delta r}{2r}\right) \frac{(\bar{v}_r)_{i,j}}{\Delta r} + \frac{2}{Re(\Delta Z)^2} + \frac{2}{1 - \frac{\Delta r}{2r}} \cdot \frac{1}{Re(\Delta r)^2} \right]^{-1} , \tag{26}$$

when the mean velocities $(\bar{v}_Z)_{i,j}$ and $(\bar{v}_r)_{i,j}$ are positive. Similar expressions for $(\Delta t)_{crit}$ are derived when $(\bar{v}_Z)_{i,j}$ and $(\bar{v}_r)_{i,j}$ are negative or they are of opposite signs. In actual computations, $\Delta t = 0.95 \times (\Delta t)_{crit}$ is used. For static stability, no restraints are imposed on spatial mesh sizes. In Figure 2, under the prescribed conditions, numerical experiments have been carried out for $\Delta r = 0.015$, 0.025, and $\alpha = 2.0$; and $\Delta r = 0.035$ and $\alpha = 2.5$, ΔZ being equal to $(2\Delta r)$ in each case. Figure 2 shows that under the prescribed conditions as the mesh size increases, gross quantities such as core growth, maximum tangential velocity decay and axial velocity distribution remain almost the same. The slight increase in axial velocity and core growth for $\Delta r = 0.035$ is primarily due to increased value of α. Numerical experiments have also been carried out with larger numbers of meshes in axial and radial directions. Increasing the mesh numbers in r and Z directions does not have appreciable effects on the flow structure so long as the prescribed conditions at the inflow section (i.e., α, Δ and core radius r) are mild and the value of the swirl ratio is low.

By suitably changing the inflow conditions, the values of the governing parameters, and by increasing the number of iterations, it is possible to remove kinks in the azimuthal components of the velocity, oscillations of the axial velocity on the axis, and relatively large variations of the flow quantities a few grid points inwards from the outflow section.

As the computations proceed in time, the flow develops smoothly from some initial state to the asymptotic steady state. In general, the criterion used to determine the steady state is as follows:

$$\max_{i,j} \left| \eta_{i,j}^{n+1} - \eta_{i,j}^{n} \right| \leq 10^{-4} \quad . \tag{27}$$

It is found that the equation for circulation converges faster than the vorticity equation. Also, the Poisson equation for ψ takes a lesser number of iterations at each time step as the solution converges.

With an exponentially varying circulation at the inflow section, the number of iterations increases excessively to get steady state solutions satisfying the previously mentioned criterion. The number of required iterations increases further as the swirl ratio is increased. However, the values of the flow quantities do not change appreciably after

$$\max_{i,j} \left| \eta_{i,j}^{n+1} - \eta_{i,j}^{n} \right| \leq 0.0005 \quad . \tag{28}$$

To save computer time without losing much accuracy, we adopt the previously mentioned criterion of convergence when the initial circulation is described by the exponential law.

The basic equations were integrated on the Univac 1108 and IBM 360 computers of MSFC. Depending on the severity of the parameters and model of the flow, typical run times varied from 15 to 125 minutes.

IV. DISCUSSION OF NUMERICAL BOUNDARY CONDITIONS AT THE OUTFLOW SECTION AND AT THE OUTER EDGE OF THE TRAILING VORTEX

Extensive numerical experiments were carried out with different conditions at the outflow section and at the outer edge of the trailing vortex to understand their effect on the detailed structure of the flow.

At the outflow section, $Z = Z_2$, the following conditions were used:

(1) $$\psi_{I,j} = 2\psi_{I-1,j} - \psi_{I-2,j} \tag{29}$$

$$\left.\frac{\partial \Gamma}{\partial Z}\right|_{I,j} = 0$$

(a) $$\left.\frac{\partial v_r}{\partial Z}\right|_{I,j} = -\frac{1}{r}\left.\frac{\partial^2 \psi}{\partial Z^2}\right|_{I,j} = 0$$

$$\therefore \eta_{I,j} = -\frac{\partial}{\partial r}\left(\frac{1}{r}\frac{\partial \psi}{\partial r}\right) \tag{30}$$

or

$$\text{(b)} \quad v_r = -\frac{1}{r}\frac{\partial\psi}{\partial Z} \quad , \quad v_Z = \frac{1}{r}\frac{\partial\psi}{\partial r}$$

$$\therefore \eta_{I,j} = \frac{\partial v_r}{\partial Z} - \frac{\partial v_Z}{\partial r} \tag{31}$$

In each case, at $Z = Z_2$, derivatives were approximated by a first order backward finite difference scheme.

$$\text{(2)} \quad \left.\frac{\partial\Gamma}{\partial Z}\right|_{I,j} = \left.\frac{\partial\psi}{\partial Z}\right|_{I,j} = 0 \tag{32}$$

v_r, v_Z, and η are computed from ψ.

In general, it is found that the numerical conditions at the outflow section do not exercise any significant effect on the rate of convergence and the upstream structure of the flow. In the present computations, boundary conditions set in (1)(a) are employed.

Similar numerical experiments have been carried out with different numerical conditions at the outer edge of the trailing vortex. Particular attention is given to the following conditions on ψ:

$$\text{(a)} \quad (\psi)_{\substack{\text{outer edge for all i} \\ \eta = 0\cdot 0}} = (\psi)_{\substack{\text{outer edge at the inflow section} \\ v_r = 0\cdot 0, \quad v_Z = 1}}$$

$$\text{(b)} \quad \psi_{i,J} = 2\psi_{i,J-1} - \psi_{i,J-2} \quad .$$

Here, v_r, v_Z, and η are approximated from the updated value of ψ by a first order backward finite difference scheme.

Condition (a) simulates the condition of a frictionless moving wall which forbids the development of a boundary layer on its surface. Most of the numerical computations thus far have been carried out with this condition based on the belief that the wall is sufficiently far from the axis and that in a sizable region of flow between the axis and the wall a uniform flow exists. As such, the

presence of the frictionless moving wall will not affect the development of the flow in the trailing vortex. Conditions in (b) update the stream function in each iteration, and thus permit the inflow and outflow of fluid at the boundary. This simulates more realistically the condition in actual flows. Numerical experiments were carried out with logarithmic and exponential laws of circulation, with boundary conditions at the outer edge prescribed in (a) or (b). It is found that conditions (b) are highly destabilizing. In several cases, computations in successive iterations converged up to a certain extent and then diverged or oscillated. Variation of mesh size or their number, changing the time interval and modifying other conditions at the edge and at the outflow section, did not improve the situation. We obtained results that satisfied our convergence criterion given in equation (27) in only one case. In Figures 3 and 4, we compare the results for axial velocity distribution on the axis and the maximum tangential velocity variation with distance downstream when conditions (a) or (b) are imposed. We find significant differences, both quantitatively and qualitatively, in the gross quantities as well as in the detailed structure of the flow. If these results are reliable, they indicate that no matter how far the outer edge is located from the axis, the prescribed conditions on it exercise significant effects on the structure of the trailing vortex.

With the conditions (a) at the outer edge, we obtain convergent solutions with Hoffman and Joubert's law of circulation for low values of swirl ratio, and with the exponential law of circulation for all values of swirl ratio. In the latter case, computation time increased excessively as the swirl ratio was increased. Also, the deceleration of the fluid on the axis is slow indicating the need of much larger range of integration if we are to obtain bursting through reversal of the flow on the axis. Thus, to get more meaningful numerical results, we need a larger computer and more computer time. Since our interest is focused on understanding the bursting phenomenon, we subsequently imposed an adverse pressure gradient in the ambient fluid to accentuate the deceleration of the flow on the axis.

V. DISCUSSION OF RESULTS

Numerical solutions of full Navier-Stokes equations are obtained for a wide range of governing parameters and prescribed conditions. At the inflow section, Hoffman and Joubert's law of circulation together with other conditions (as stated in Section II) are prescribed. These conditions at the inflow section introduce the following parameters in the problem:

1. Radius r_1 of the core where the azimuthal component of velocity reaches its maximum.

2. Distance from the axis at which the axial velocity matches the ambient velocity.

3. Deficit or excess Δ in axial velocity on the axis. Other parameters appearing in the basic equations are the swirl ratio and the Reynolds number.

In the following discussion, we shall try to understand the manner in which the flow pattern in the trailing vortex changes as we vary a parameter while others remain fixed.

In Figures 5 and 6 we compute the flow with an excess or deficit in the axial velocity on the axis at the inflow section when Re = 2000, swirl ratio = 0.2, core radius = 0.1, and $\alpha = 2.5$. $v_Z(Z_1, 0)$ changes from 0.4 to 1.576. From Figure 5, we find that with an excess axial velocity, the flow on the axis decelerates while with a deficit axial velocity the flow accelerates in the downstream direction. With an almost uniform flow at the inflow section, the flow remains almost uniform in the downstream direction. This feature of the flow is in general agreement with the available experimental data [11-14]. From Figure 6, we observe that as the magnitude of the axial velocity decreases, the maximum tangential velocity also decreases. There is hardly any change in the core growth as a result of the changes in the axial velocity on the axis at the inflow section.

In Figure 7, we compare the variations in the axial velocity on the axis, maximum tangential velocity, and core growth as a result of the changes in core radius, r_1, from 0.05 to 0.25 when Re = 2000, swirl ratio = 0.2, $v_Z(Z_1, 0) = 1.176$, and $\alpha = 2.5$. We find that as the inflow core radius increases from 0.05 to 0.25 in steps of 0.05, the flow accelerates, maximum tangential velocity decays slower, and the rate of growth of the core decreases. This leads us to believe that a trailing vortex with a larger inflow core radius will persist longer. We further observe that the changes in $v_Z(Z_1, 0)$ and $[(v_\varphi)_{max}/V_1]$ are more pronounced for smaller values of the core radius. Under the prescribed conditions, there is hardly any change in $v_Z(Z, 0)$ when the core radius is greater than 0.15.

In Figure 8, profiles are drawn for the tangential velocity distribution as the inflow core radius becomes 0.1, 0.2, and 0.25 with Re = 2000, swirl ratio = 0.2, and $\alpha = 2.5$. We find that there is no kink in the v_φ-profile for a core radius of 0.1. A kink in v_φ-profile appears when the core radius equals 0.2. The magnitude of the kink increases as the core radius increases to 0.25.

In Figure 9, we compare $v_Z(Z, 0)$ and $[(v_\varphi)_{max}/V_1]$ when $\alpha = 1.0$, 2.0, Re = 2000, swirl ratio = 0.2, inflow core radius = 0.105, and $v_Z(Z_1, 0) = 1.176$. We find that as α increases, axial velocity increases and $[(v_\varphi/V_1)_{max}]$ decreases slightly. An important feature is that the slight overshoots in $[(v_\varphi)_{max}/V_1]$ in the entrance region with $\alpha = 1.0$ smears away when $\alpha = 2.0$.

In Figures 10 and 11, we compare axial velocity and maximum tangential velocity distributions with changes in Reynolds number when swirl ratio = 0.2, core radius = 0.1, $\alpha = 2.5$, and $v_Z(Z_1, 0) = 0.75$ or 1.25. Figure 10 indicates that with an excess inflow axial velocity, $v_Z(Z, 0)$ increases with Reynolds number, while the opposite trend prevails with a deficit inflow axial velocity. Larger variations in the entrance region can be corrected by suitably changing other parameters. No rational explanation can be obtained for this opposite effect of Reynolds number on $v_Z(Z, 0)$ with an excess or deficit inflow axial velocity. Figure 11 presents graphs for $[(v_\varphi)_{max}/V_1]$ with a deficit or an excess inflow axial velocity. Reynolds number changes from 5000 to 15 000. We find that in all cases the maximum tangential velocity decays slower and the core becomes more slender as the Reynolds number increases. The latter results show that a trailing vortex with a greater Reynolds number may persist longer before dissipation.

Figures 12 and 13 present graphs for the various flow quantities with an excess and deficit inflow axial velocities when Re = 2000, core radius = 0.1, and $\alpha = 2.5$. In Figure 12, $v_Z(Z_1, 0) = 1.176$ and the swirl ratio takes values of 0.0, 0.2, and 0.4. We find that the axial velocity decreases and $[(v_\varphi)_{max}/V_1]$ and the core growth remain unaffected as the swirl ratio increases. Figure 13 indicates that with a deficit inflow axial velocity $v_Z(Z_1, 0) = 0.75$ and swirl

ratio = 0.4, $v_Z(Z, 0)$ decreases continuously except for a slight rise in its value at the entrance region. For swirl ratio = 0.6, $v_Z(Z, 0)$ decreases initially and then increases slightly as the outflow end is reached. There is a slight decrease in $[(v_\varphi)_{max}/V_1]$ as the swirl ratio increases from 0.4 to 0.6. No appreciable change in core growth is noticed with the increase in swirl ratio. As the swirl ratio was further increased to 0.8, we could not obtain a convergent solution even after a 70 minute run of the Univac 1108 computer. Successive values of

$$[\Delta\eta]_{\substack{max \\ i,j}} = \left| \eta_{new} - \eta_{old} \right|_{i,j}$$

oscillated, indicating either convergence was not possible or it would take too long.

This discussion shows that, in general, the swirl ratio has an effect similar to the adverse pressure gradient. It can be traced directly in the vorticity equation when the swirl ratio is associated with the circulation gradient term which is negative so long as the core expands. It plays a crucial role in determining whether a breakdown is a possible phenomenon and the manner in which a trailing vortex dissipates. Our findings from past investigations are as follows:

1. With Hoffman and Joubert's law of circulation, we could not get bursting through the stagnation of the fluid on the axis and the consequent reversal of the flow. More numerical experiments are probably needed to reach this conclusion decisively.

2. Trailing vortices do not decay like the viscous vortex predicted by Newman, viz. $(v_\varphi)_{max} \propto (1/\sqrt{Z})$ and $(r_1/C) \propto \sqrt{Z}$.

3. Trailing vortices persist too long or too far downstream.

It may also be noted that the flow downstream depends critically on the conditions at the inflow section and the governing parameters. It has a large number of parameters which have opposite effects on the flow structure. It may be difficult to derive any general conclusions. The previously mentioned

parametric study only gives us some idea of how the flow pattern should change when one parameter changes and others are kept constant.

Let us now compare our theoretical predictions with the experimental data of Chigier and Corsiglia [12] in 7 by 10 ft tunnel of NASA's Ames Research Center. These measurements were made with the Convair 990 wing model and with a rectangular wing. These data have certain typical features generally found in the measurements of other investigators. Distinguishing features of the flow on the two wings are as follows:

1. In the Convair 990 wing model tests, we observe that a deficit axial flow at the inflow section $(Z'/C = 6)$ accelerates to an almost uniform flow at the outflow section $(Z'/C = 12)$. Axial profile merges with the ambient flow just outside the core.

2. In the rectangular wing tests, we see that an excess axial velocity on the axis at $Z'/C = 4$ decelerates to an almost uniform flow at $Z'/C = 9$. Axial velocity attains the ambient velocity at a distance approximately twice the radius of the core.

Chigier and Corsiglia [12] documented the data for transverse and spanwise traverses. In certain cases, there are appreciable differences in the measurements of the two traverses. These differences are probably due to the presence of a secondary vortex besides the primary trailing vortex. The data which are markedly affected by the presence of the secondary vortex are not included in the comparison. However, some data which bear slight effect of the secondary vortex are included in the graphs. At the initial section, an average value of the core radius r_1, maximum tangential velocity V_1, and the excess or deficit axial velocity on the axis is taken from the experimental data for our theoretical model of the flow. Kuhn and Nielson [9] found that Hoffman and Joubert's law of circulation reproduces the experimental data for both wings with reasonable accuracy. Using the eddy viscosity concept, they found the Reynolds numbers for the flows on the Convair 990 wing model and on the rectangular wing as 3333 and 2143, respectively. In our theoretical calculations, we used the same law of circulation and the Reynolds numbers. For the sake of uniformity and to incorporate more points in the core area, we have taken the mid-chord $C = 1.0$.

In Figure 14, we compared the theoretical predictions of the core growth, the maximum tangential velocity distribution, and the axial velocity on the axis with the corresponding experimental data on the Convair 990 wing model. We found that the average value of the data is not affected markedly by the secondary vortex, and it approximates reasonably well the theoretical predictions. Figure 15 presents the tangential velocity distributions at various sections in the downstream direction. We observe a clear tendency of smearing the tangential velocity profile with the ambient fluid. Also, under the prescribed conditions of the governing parameters, there is hardly any change in the tangential velocity profile in the outer portion of the flow at the various downstream sections.

In Figures 16, 17, and 18, we compare the present results for the overall characteristics of the flow such as the axial velocity distribution on the axis, the maximum tangential velocity distribution, and the core growth with downstream direction with the corresponding experimental data. Also in Figures 19 through 22, we compare the detailed structure of the flow represented by the axial and the tangential velocity profiles with the corresponding data in the spanwise and normal traverses. In all cases, the agreement of the theoretical predictions with the experimental data seem to be within the experimental error.

Attempts were made to obtain vortex bursting in the calculations. Within Hoffman and Joubert's law of circulation, solutions diverged as the swirl ratio was increased to 0.8 with Re = 2000 and an inflow core radius of 0.4 C. We subsequently changed the circulation distribution at the inflow section to an exponentially varying law, given by equation (13), while the other conditions were kept the same. Convergent solutions resulted, but the number of iterations increased excessively. Comparative study indicates that under similar conditions convergence is faster with the logarithmic law than with the exponential law of circulation. With the exponential law, the number of iterations increases rapidly as the swirl ratio is increased.

To save computer time and obtain bursting within the capability of the available computers, it was necessary to impose an adverse pressure gradient, given by equation (14), at the outer edge of the trailing vortex so that the flow decelerates rapidly and bursting through the reversal of the flow may occur.

In Figure 23, we compare the results of axial velocity distribution on the axis of the trailing vortex when the ambient axial velocity is given by $v_Z = \Delta(1 - \beta Z)$. Here, the computations are made with $\Delta = 1.0$, $\beta = 0.0$; $\Delta = 1.0$,

$\beta = 0.2$; $\Delta = 1.0$, $\beta = 0.25$; $\Delta = 0.75$, $\beta = 0.25$; and $\Delta = 0.5$, $\beta = 0.25$ when Re = 10.0 and swirl ratio = 0.8. It is quite evident that the greater deceleration of the fluid at the outer edge of the vortex leads to larger retardation of the fluid on the axis. With a larger deficit axial flow at the inflow section, there is larger deceleration of the fluid on the axis. Comparatively larger changes take place near the inflow section. For $\Delta = 0.75$, $\beta = 0.25$, and Z = 4.0, the axial velocity at the outflow section is zero; therefore, we impose a strong adverse pressure gradient on the trailing vortex. In the other computations, $\Delta = 0.75$ and $\beta = 0.25$ are taken.

In Figure 24, we compare the axial velocity variation on the axis when the Reynolds number changes from 10 to 50 and the swirl ratio is kept constant at 0.8. We find that with increasing Reynolds number, there is larger deceleration of the fluid. Actually, bursting of the trailing vortex through the stagnation of the fluid on the axis and consequent reversal of the flow have taken place. Bursting may take place at lower values of the swirl ratio if the Reynolds number is increased. This result is similar to the one shown in Figure 10 with the Hoffman and Joubert law of circulation.

Figure 25 presents curves for the axial velocity variation on the axis with the distance downstream at swirl ratios of 0.6, 0.65, 0.7, and 0.8 with the Reynolds number equal to 50. At a swirl ratio = 0.6, $v_Z(Z, 0)$ decreases continuously to zero at the outflow section. For other values of swirl ratio, the axial velocity decreases faster in the entrance region and then increases to attain zero value at the outflow section. This deceleration is greater with larger values of the swirl ratio. It is clear that for Re = 50, bursting of the trailing vortex has taken place for a value of the swirl ratio lying between 0.6 and 0.65.

Figure 26 shows the growth of the core for the swirl ratios of 0.6, 0.65, 0.70, and 0.8 and Re = 50. The striking feature of this graph is the nonlinear growth of the core up to a certain distance downstream, followed by a sudden jump to the outer edge of the region of integration. The core radius remains constant thereafter. As the swirl ratio is increased, the core grows faster and the jump in the core growth takes place earlier. It is interesting to observe that this jump in the core radius takes place even before the bursting of the trailing vortex through the stagnation of the fluid on the axis has taken place. This abrupt change in the core growth at a particular section downstream shows that some sharp change in the flow characteristics is taking place, indicating some sort of breakdown in the sense of the Benjamin [20] and Ludwieg [21] theories. There is need to investigate the phenomenon of abrupt growth of the core through more numerical solutions of the Navier-Stokes equations and comparing them with the results of the available theories.

Figure 27 shows the variation of the maximum tangential velocity with the downstream distance for various values of the swirl ratio and Re = 50. We observe that for each value of the swirl ratio the maximum tangential velocity decreases with rapidity up to the point where the abrupt change in the core growth takes place, and then it remains constant. With the increase in swirl ratio, the ratio $[(v_\varphi)_{max}/V_1]$ decreases faster. Figure 28 presents the profiles for the tangential velocity at different stations in the downstream direction, with a swirl ratio of 0.8 and Re = 50. As we move downstream, the point of maximum tangential velocity moves towards the outer edge of the trailing vortex and the profiles become almost linear. This shows that the fluid in the downstream portion rotates like a solid body.

Figures 29 through 32 present streamlines for swirl ratios of 0.6, 0.65, 0.7, and 0.8 and Re = 50. In Figure 30, we observe the formation of a bubble. Figures 31 and 32 indicate that as the swirl ratio increases, the extent of the bubble increases in the longitudinal and transverse directions. In Reference 4, the authors obtained solutions depicting formation of eddies in a rotating tube. The present results differ from them in certain essential features.

VI. CONCLUDING REMARKS

Numerical solutions of the full Navier-Stokes equations have been obtained for the structure of a trailing vortex. Various phenomena that may occur in the trailing vortex are examined by varying the prescribed conditions and the governing parameters. Using the Hoffman and Joubert [10] law of circulation at the inflow section, the present theory predicts reasonably well the experimental data of Chigier and Corsiglia [12] on models of the Convair 990 wing and a rectangular wing. Use of an exponential law of circulation at the inflow section and an adverse pressure gradient at the outer edge of the trailing vortex lead to solutions that depict a vortex bursting through the sudden expansion of the core and through stagnation and subsequent reversal of the flow on the axis.

A better understanding of the various bursting processes that lead to the dissipation of the trailing vortex is needed. More numerical solutions of the full Navier-Stokes equations with different models of the flow should be obtained and the results be compared with available theories.

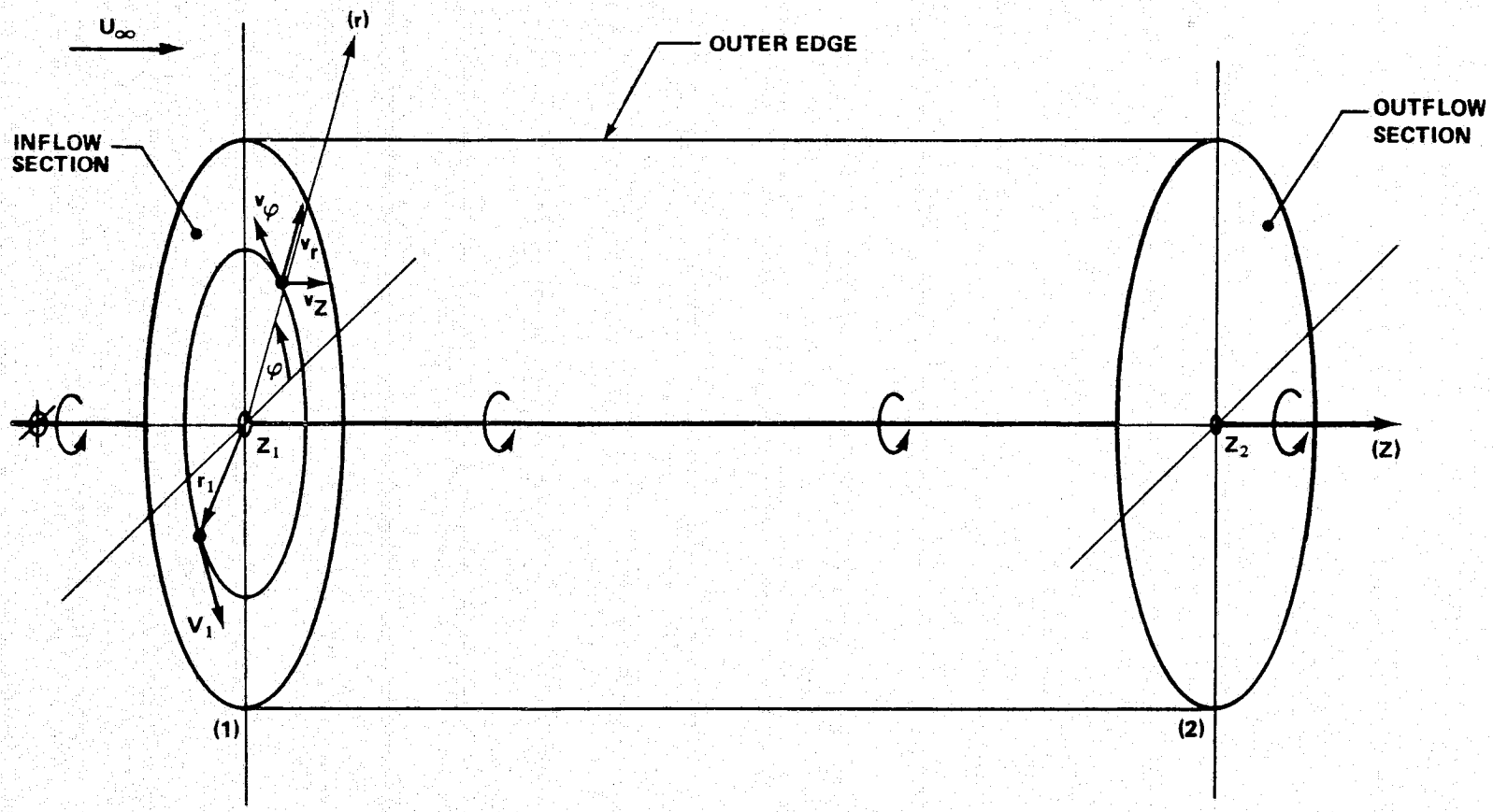

Figure 1. Coordinate system.

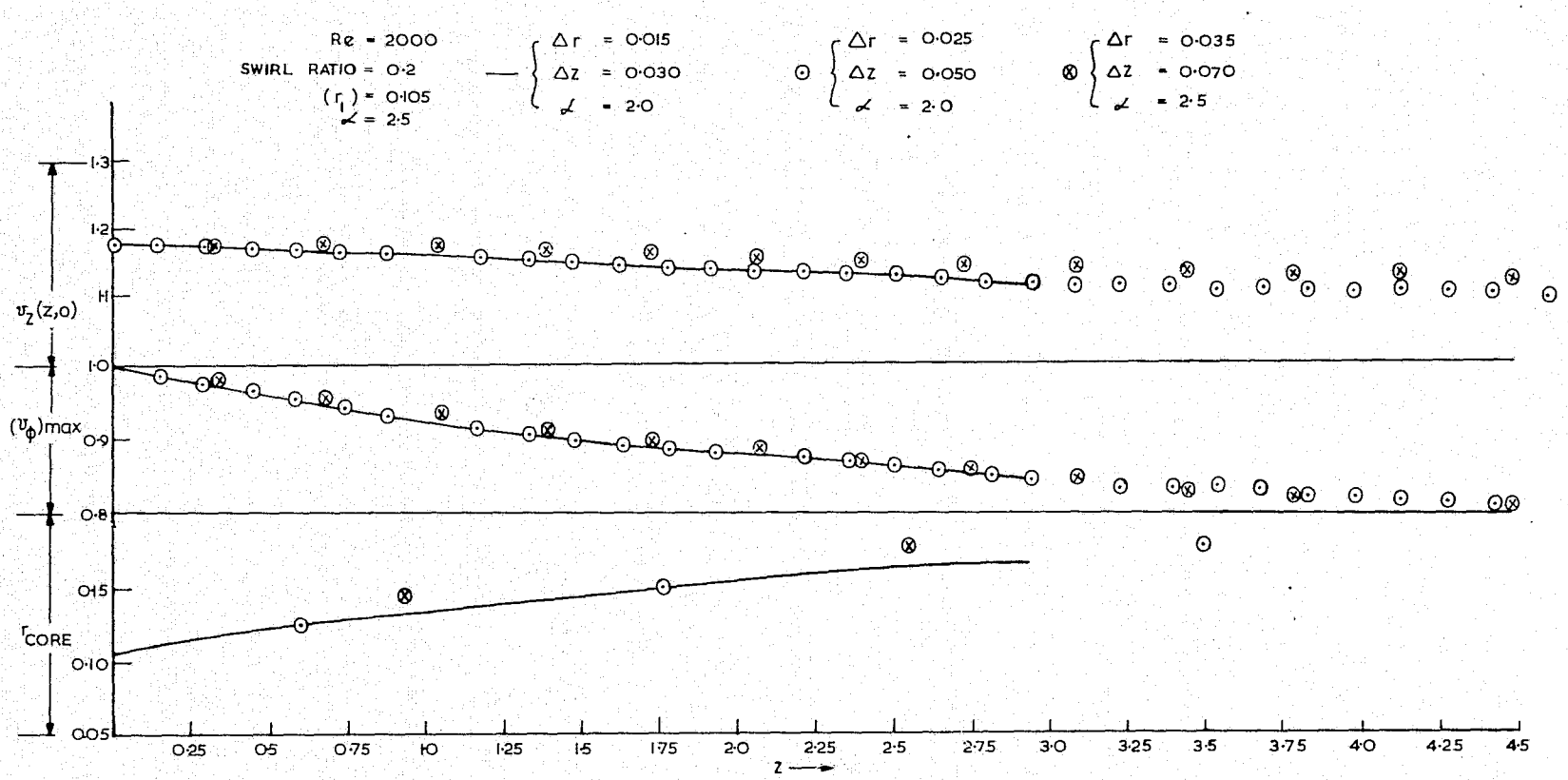

Figure 2. $v_Z(Z, 0)$, $(v_\phi)_{max}$ and r_{core} versus Z with different mesh sizes.

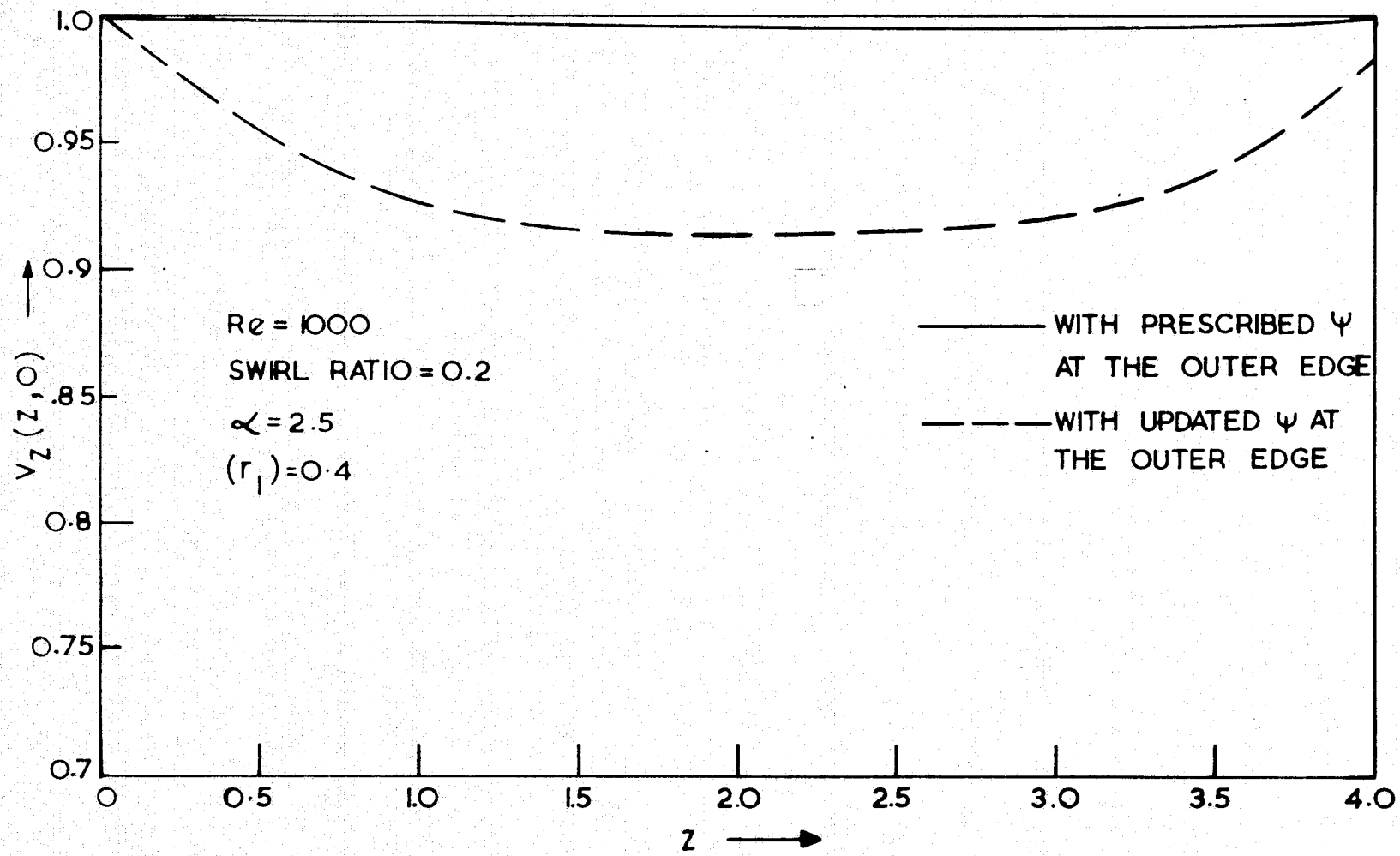

Figure 3. $v_Z(Z, 0)$ versus Z with different outer edge conditions.

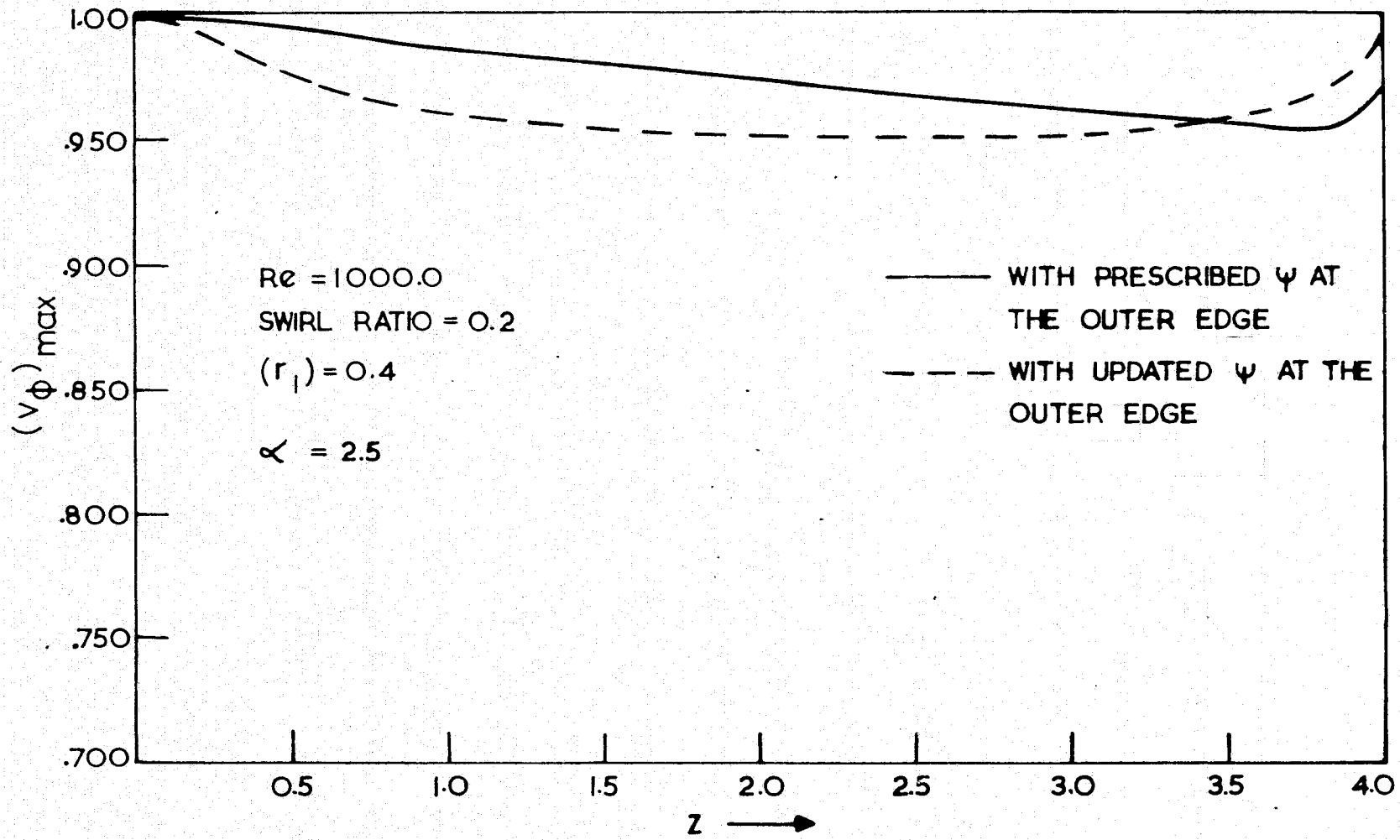

Figure 4. $(v_\phi)_{max}$ versus Z with different outer edge conditions.

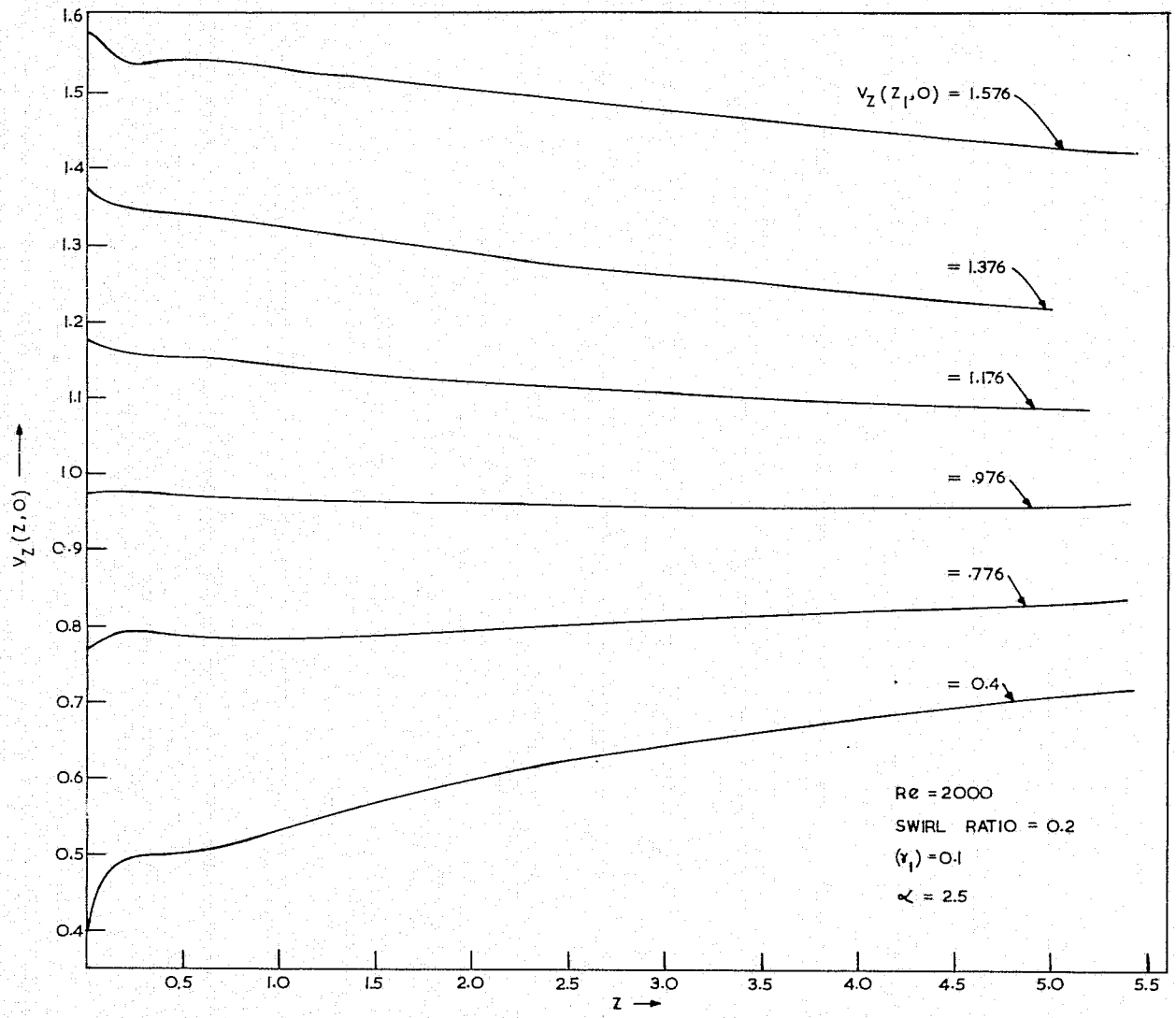

Figure 5. $v_Z(Z, 0)$ versus Z for different $v_Z(Z_1, 0)$.

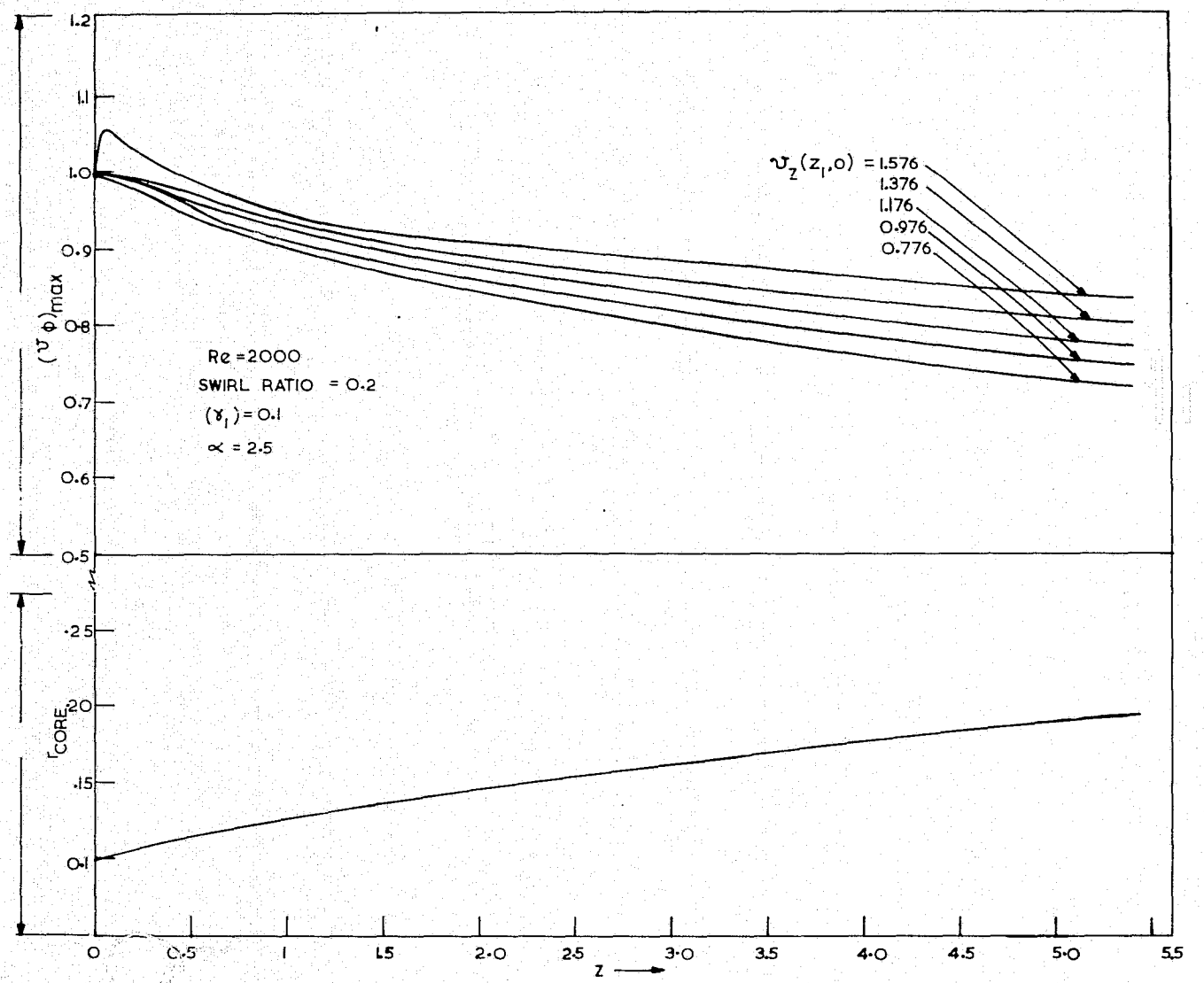

Figure 6. $(v_\phi)_{max}$ and core growth, r_{core}, versus Z for different $v_Z(Z_1, 0)$.

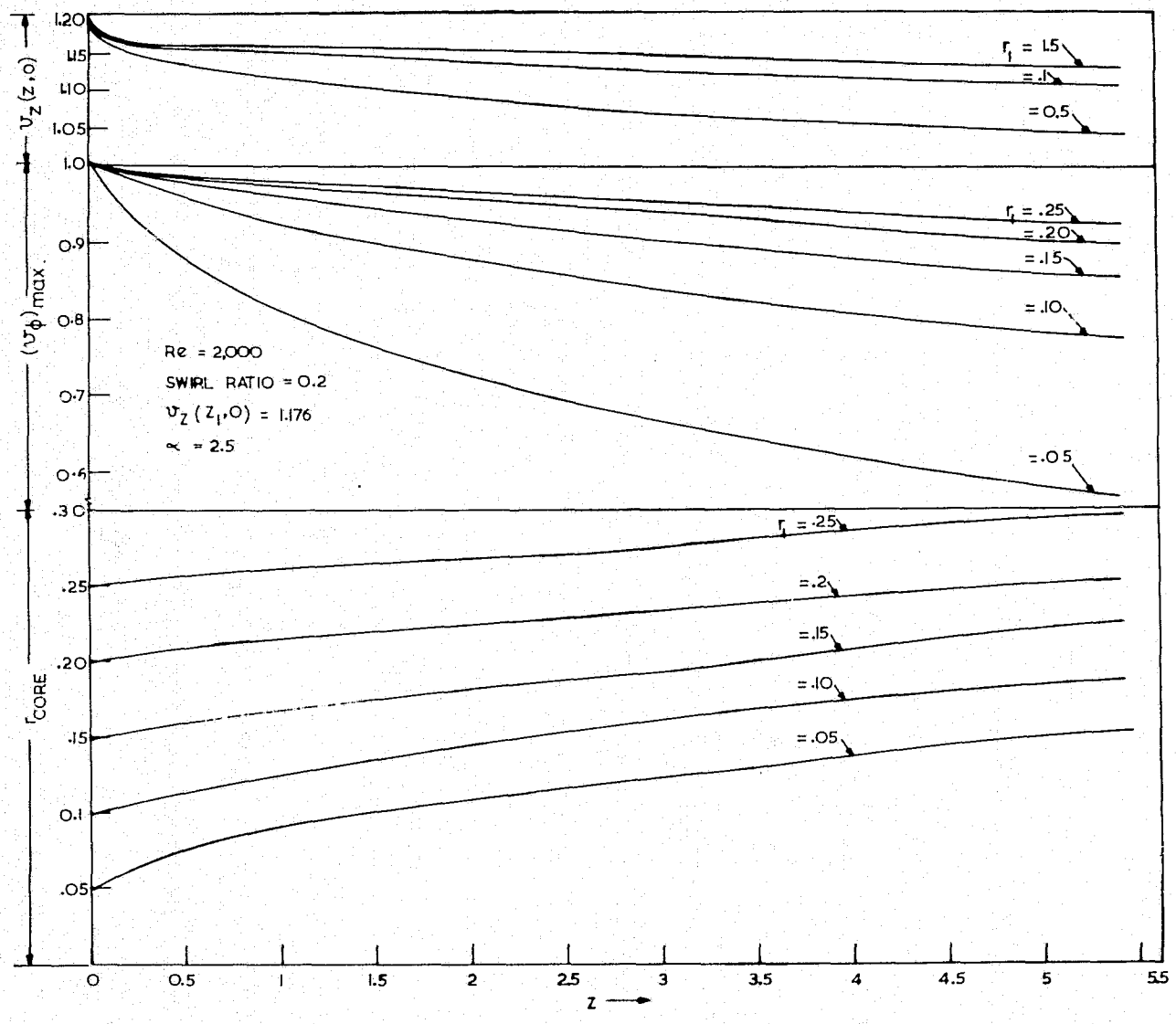

Figure 7. $v_Z(Z, 0)$, $(v_\phi)_{max}$ and γ_{core} versus Z for different values of core radius at inflow section.

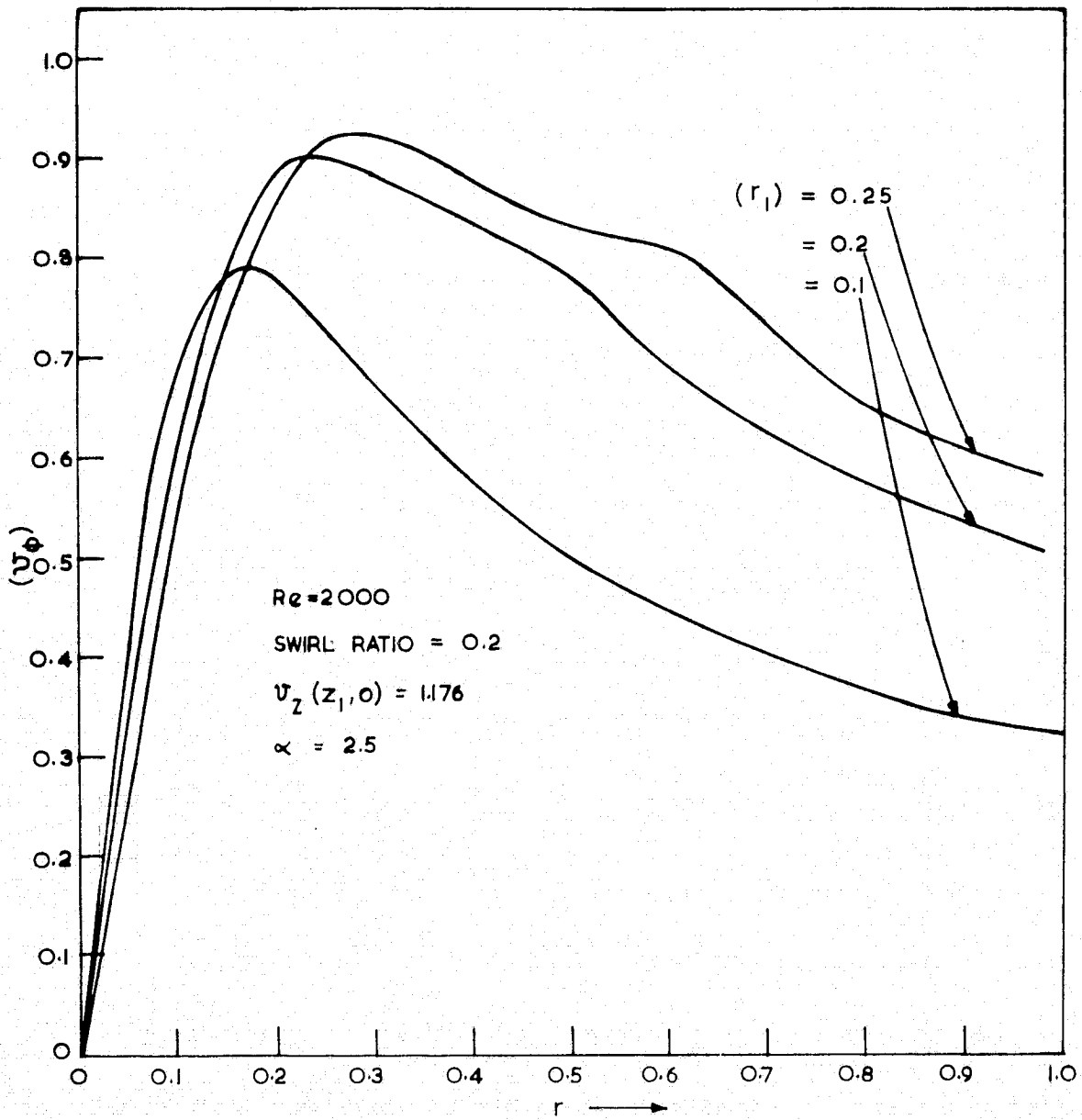

Figure 8. v_ϕ versus radial distance 'r' at Z = 5.0 for different (r_1).

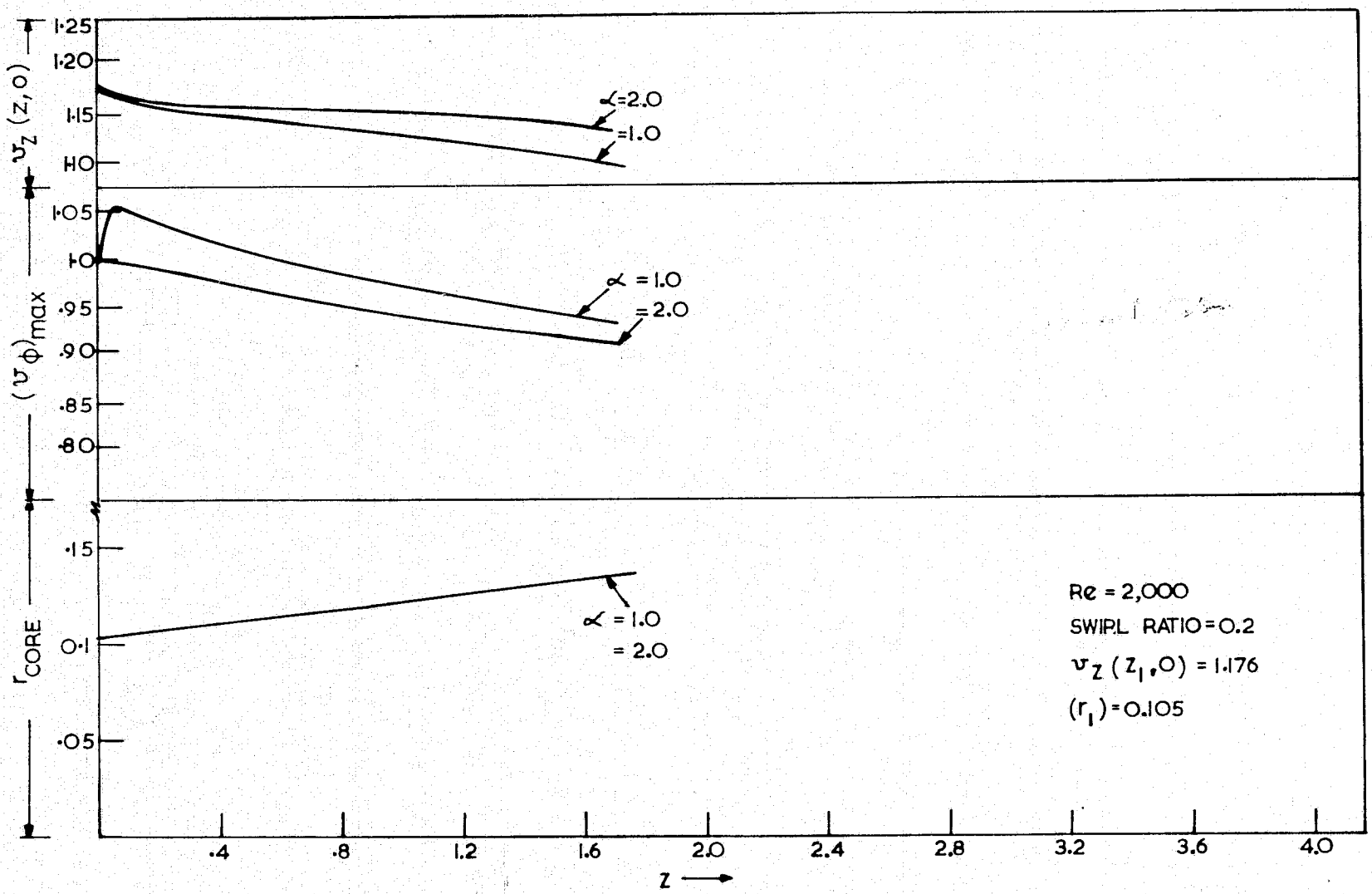

Figure 9. $v_Z(Z, 0)$, $(v_\phi)_{max}$ and core growth, r_{core}, versus 'Z' for different values of 'α'.

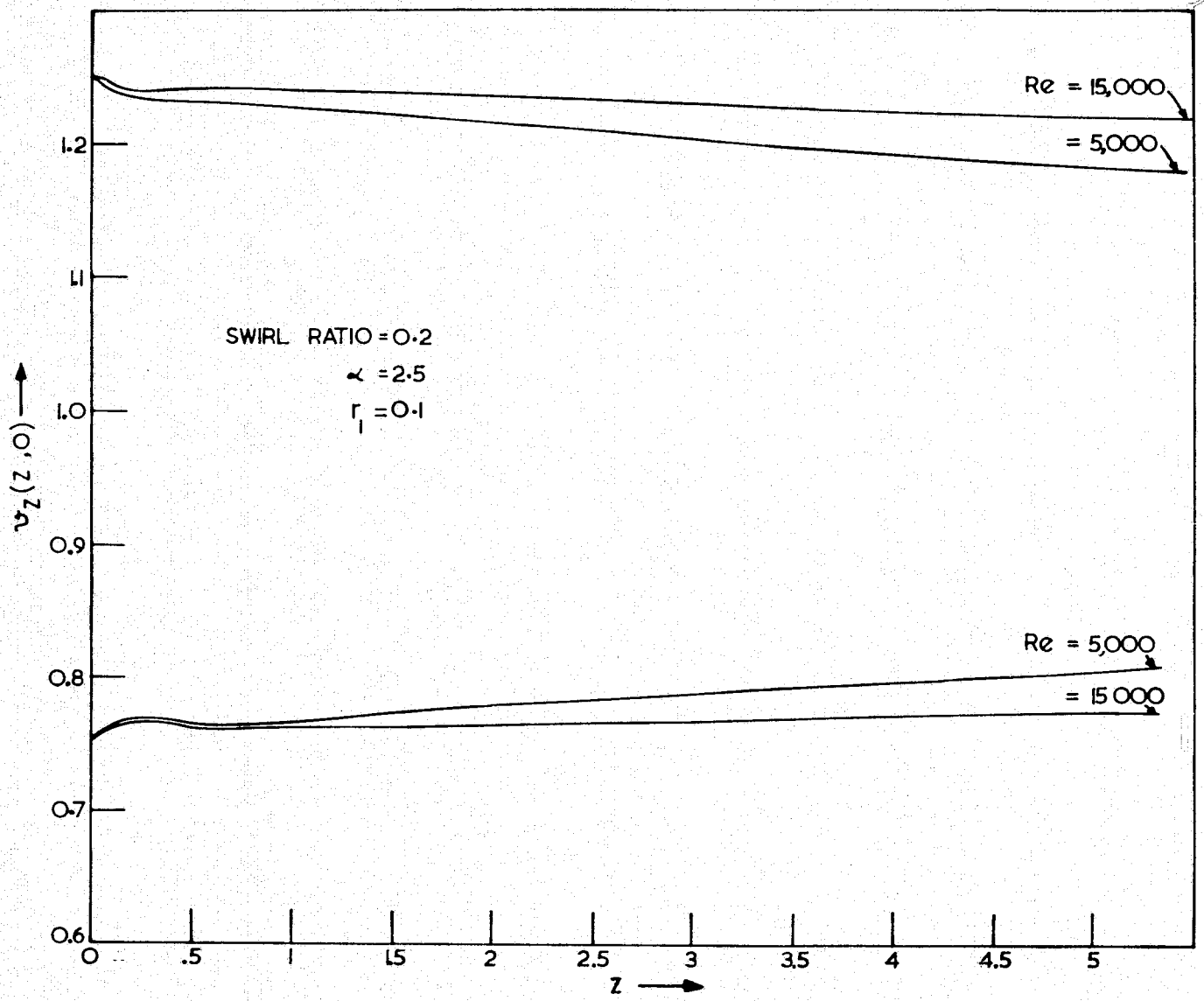

Figure 10. $v_Z(Z, 0)$ versus Z for different values of Reynolds number.

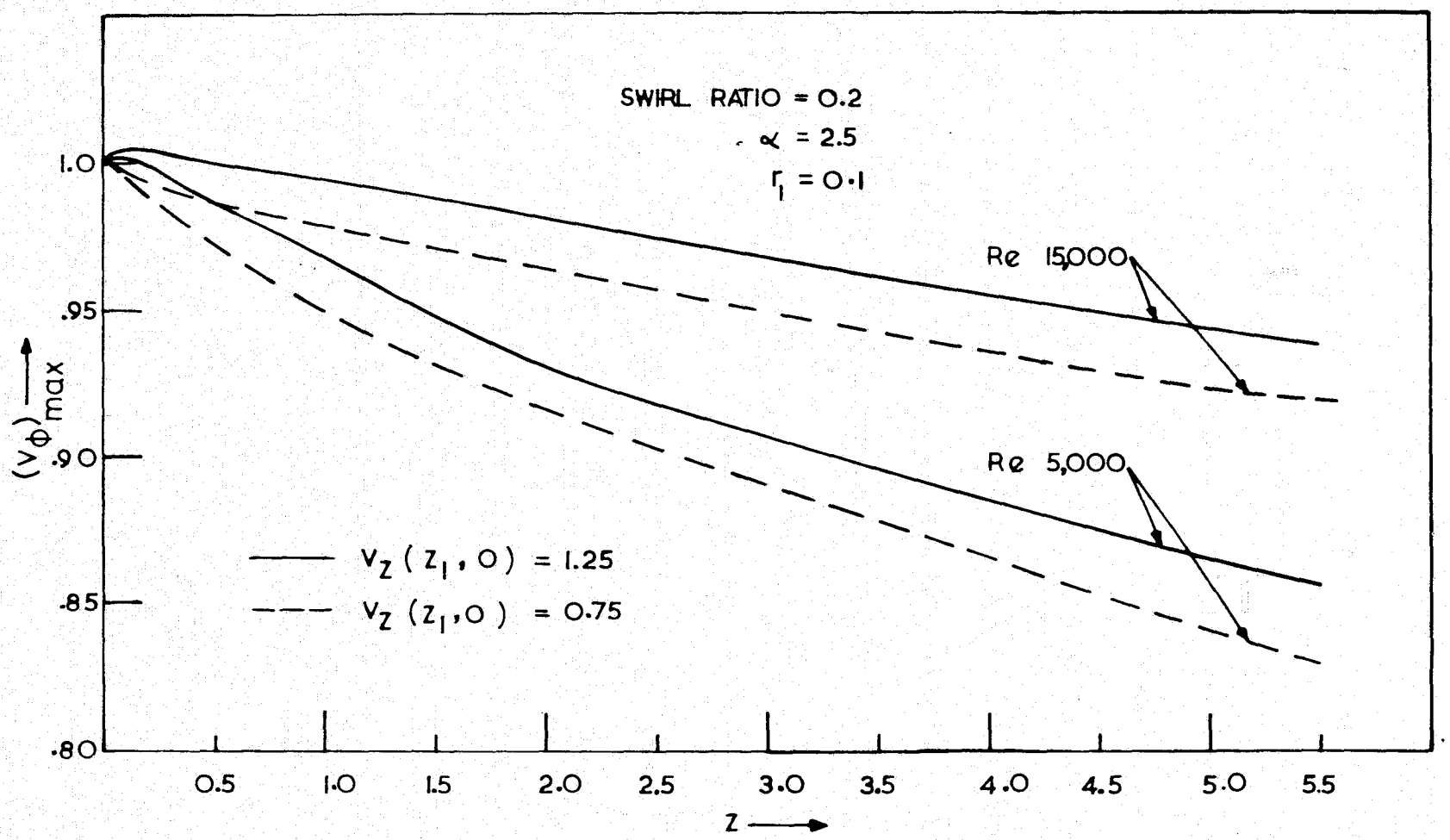

Figure 11. $(v_\phi)_{max}$ versus Z for different values of Reynolds number.

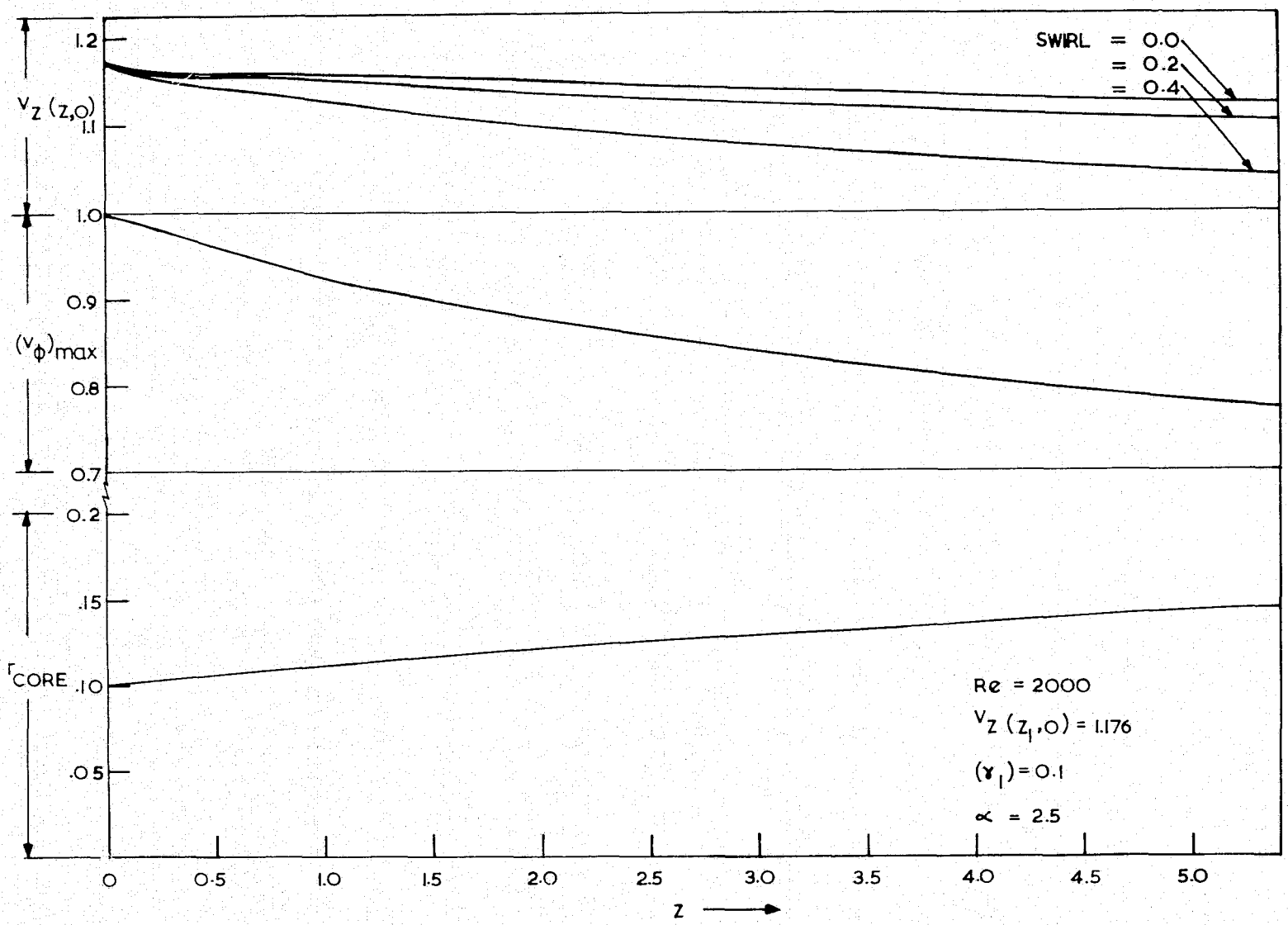

Figure 12. $v_Z(Z, 0)$, $(v_\phi)_{max}$ and, r_{core}, versus 'Z' for different values of swirl ratio.

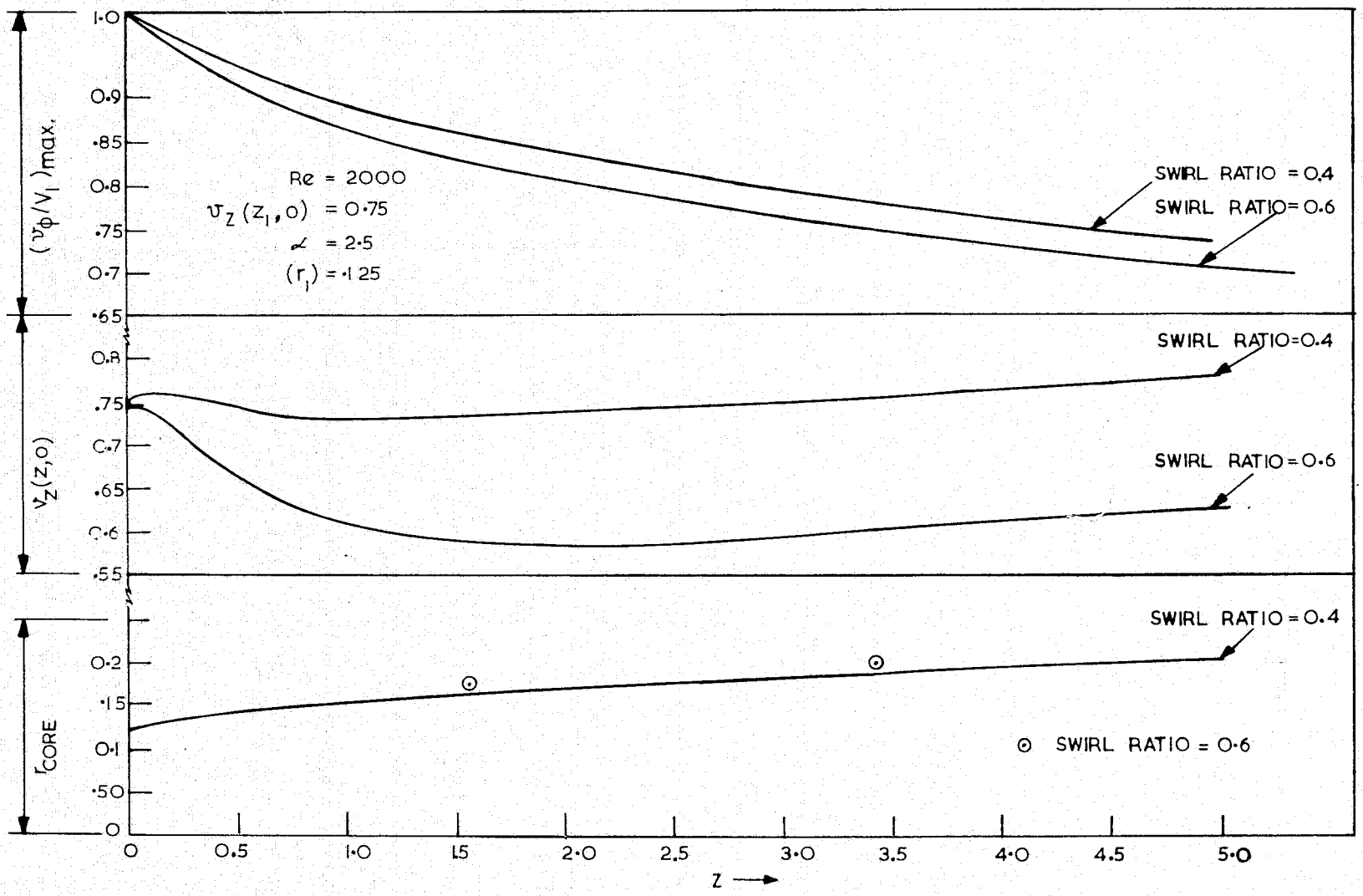

Figure 13. $(v_\phi/V_1)_{max}$, $v_Z(Z, 0)$ and core growth, r_{core}, versus 'Z' for different values of swirl ratio.

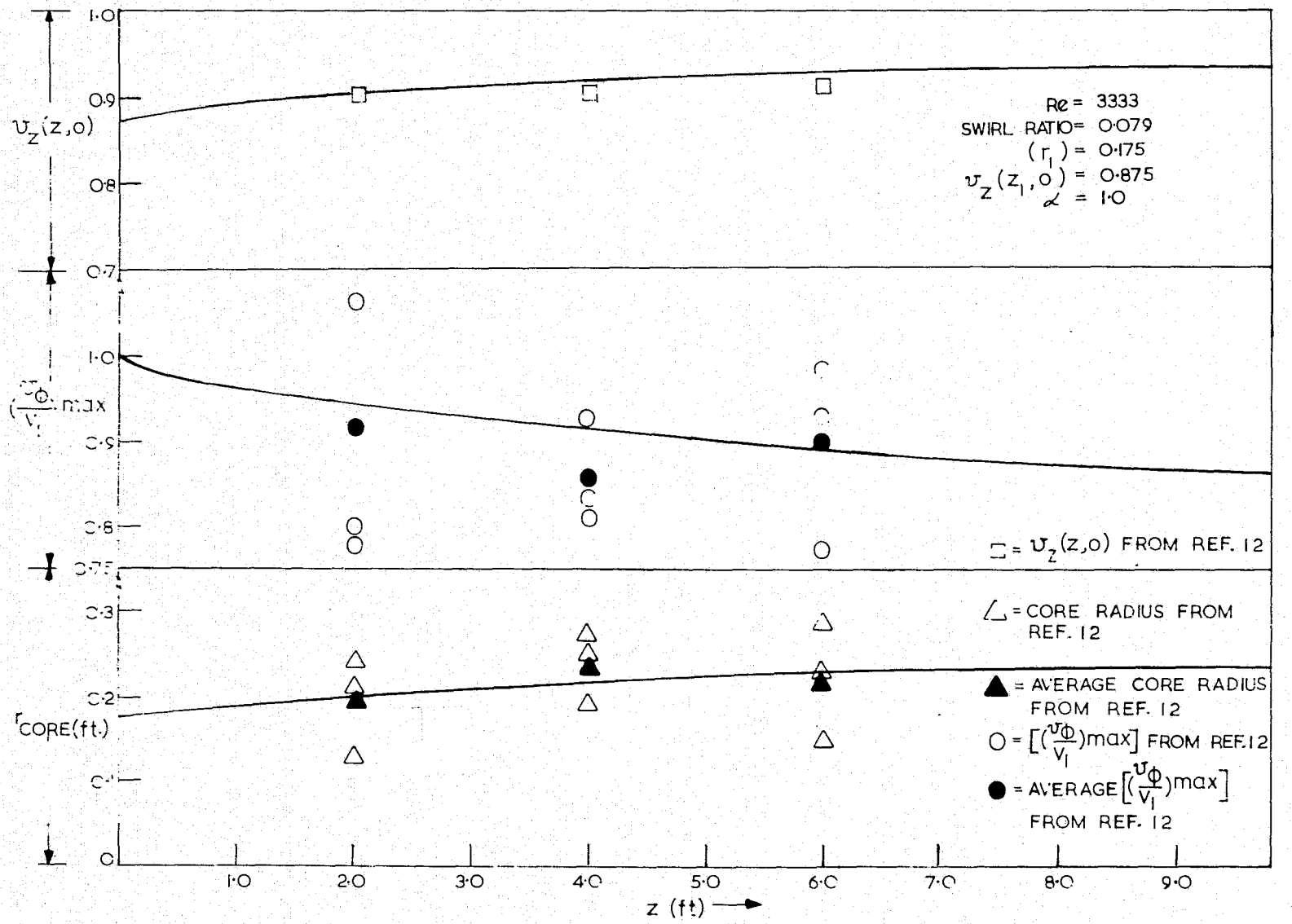

Figure 14. Comparison of the present results of $v_Z(Z, 0)$, $(v_\phi / V_1)_{max}$ and, r_{core}, versus 'Z' with corresponding experimental data of Reference 12.

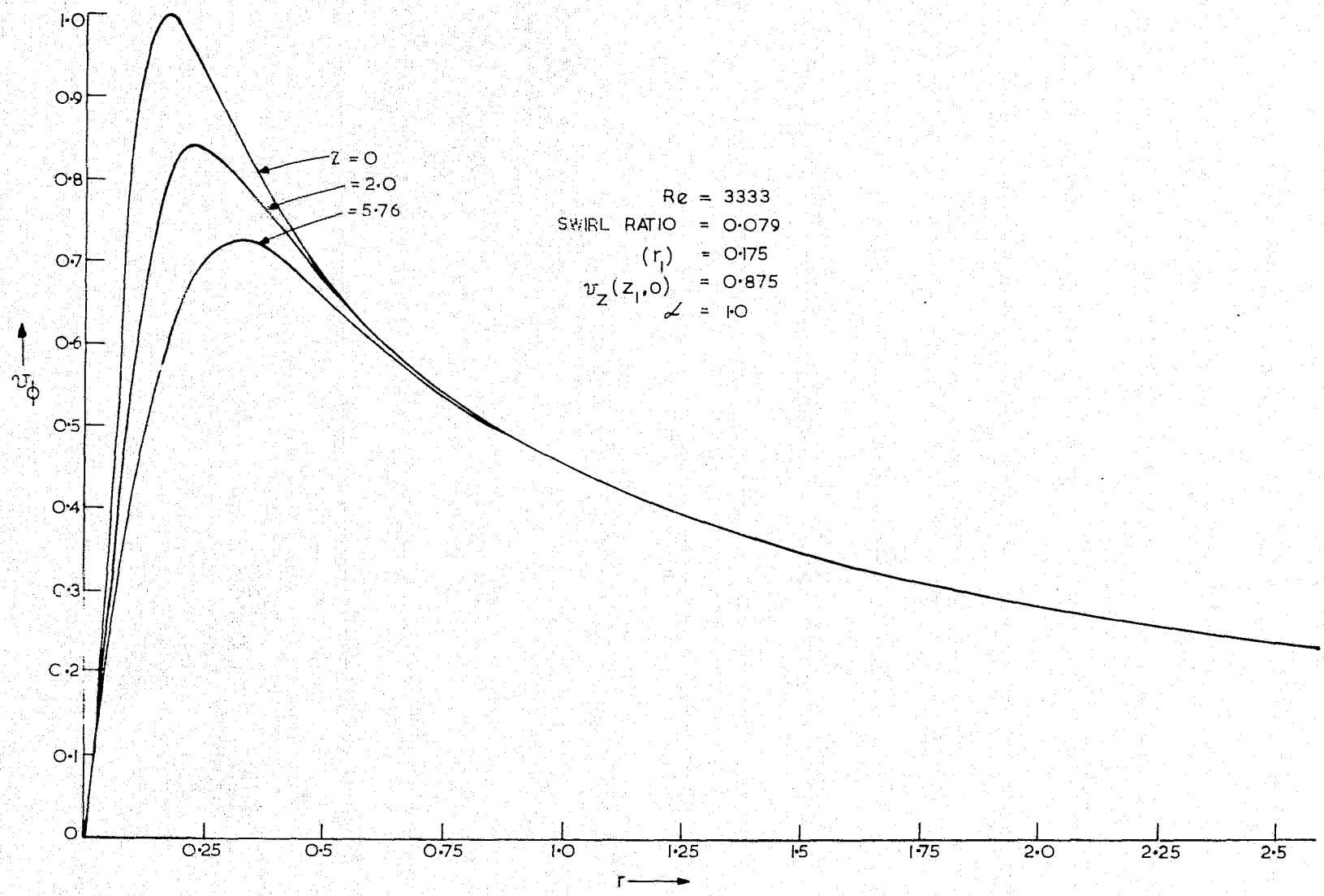

Figure 15. v_ϕ versus r at various sections in downstream direction.

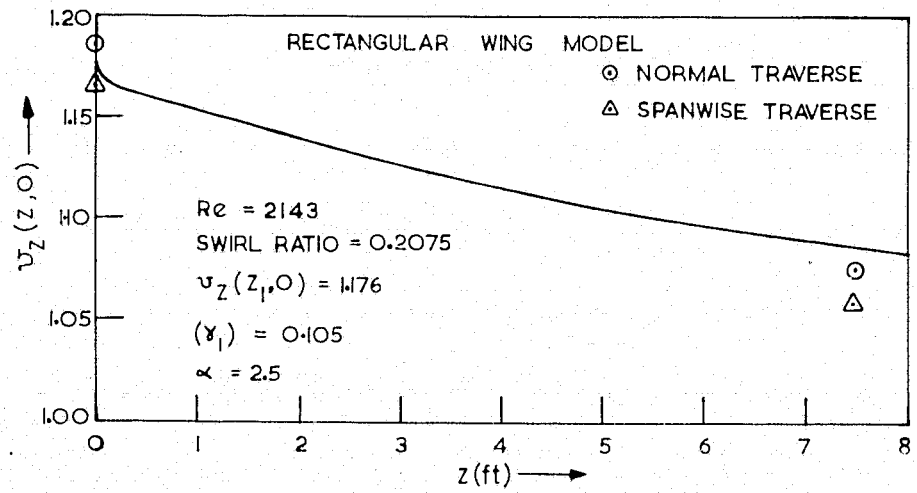

Figure 16. Comparison of the present results for $v_Z(Z, 0)$ versus Z with the experimental data of Reference 12.

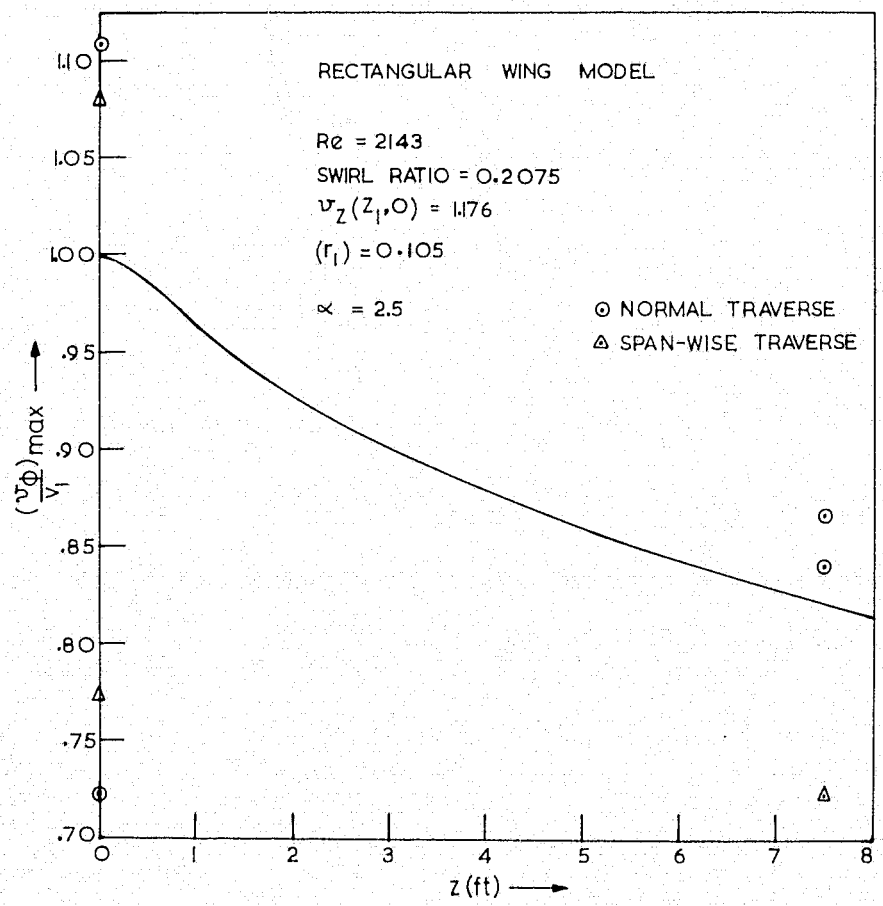

Figure 17. Comparison of the present results for $(v_\phi / V_1)_{max}$ versus Z with the experimental data of Reference 12.

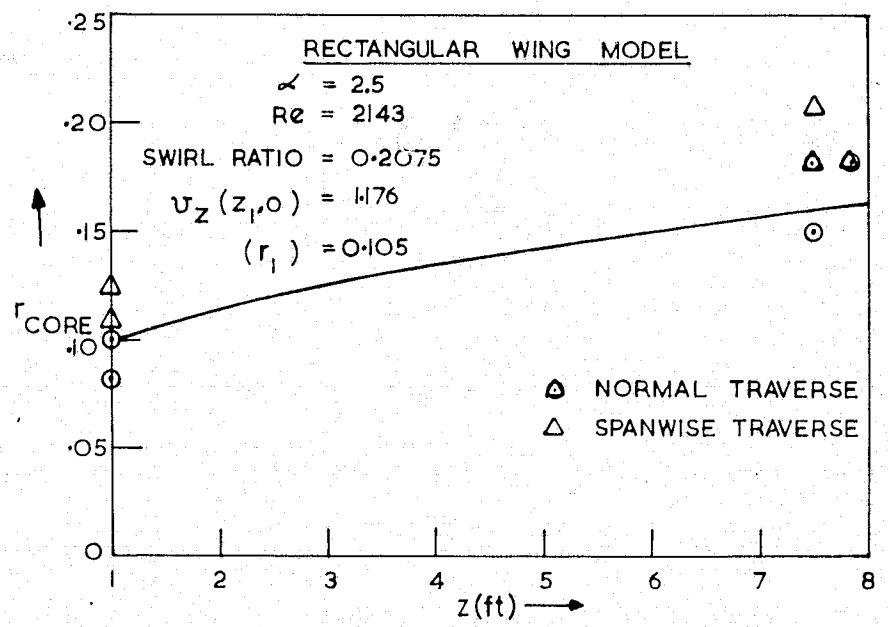

Figure 18. Comparison of present results for core growth r_{core} versus Z with the experimental data of Reference 12.

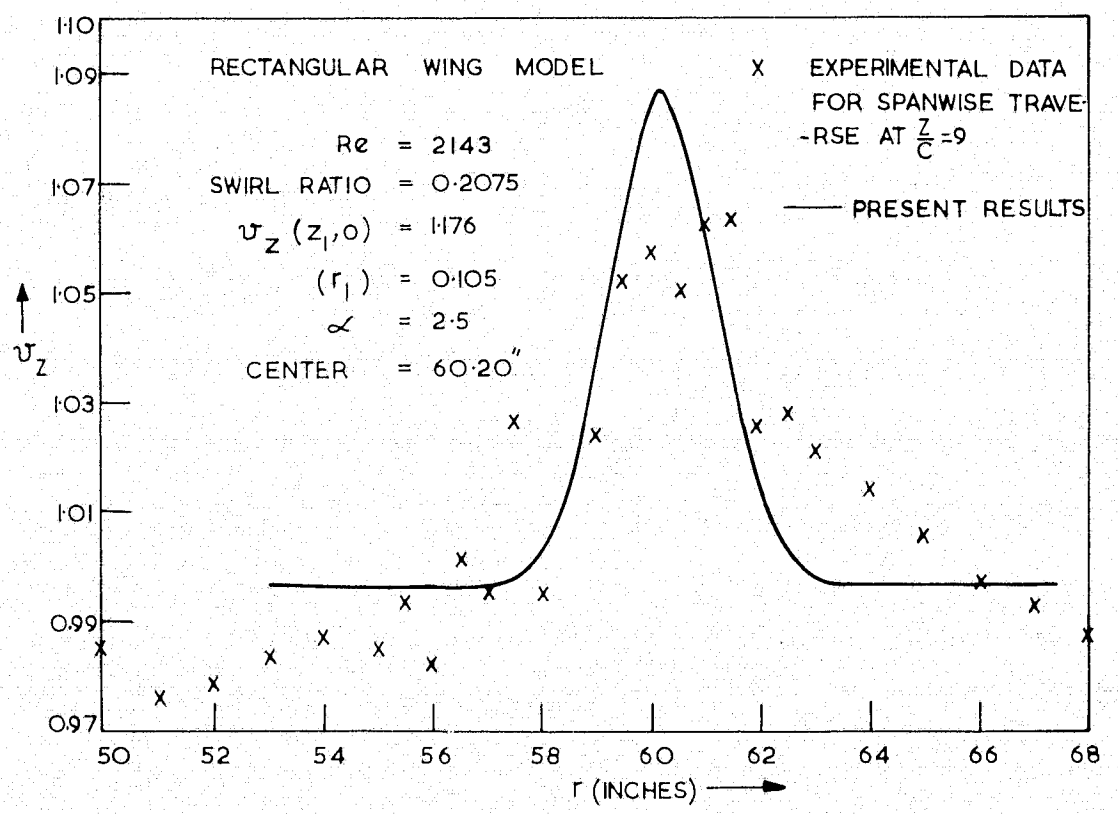

Figure 19. Comparison of the present results for v_Z versus r with the experimental data of Reference 12.

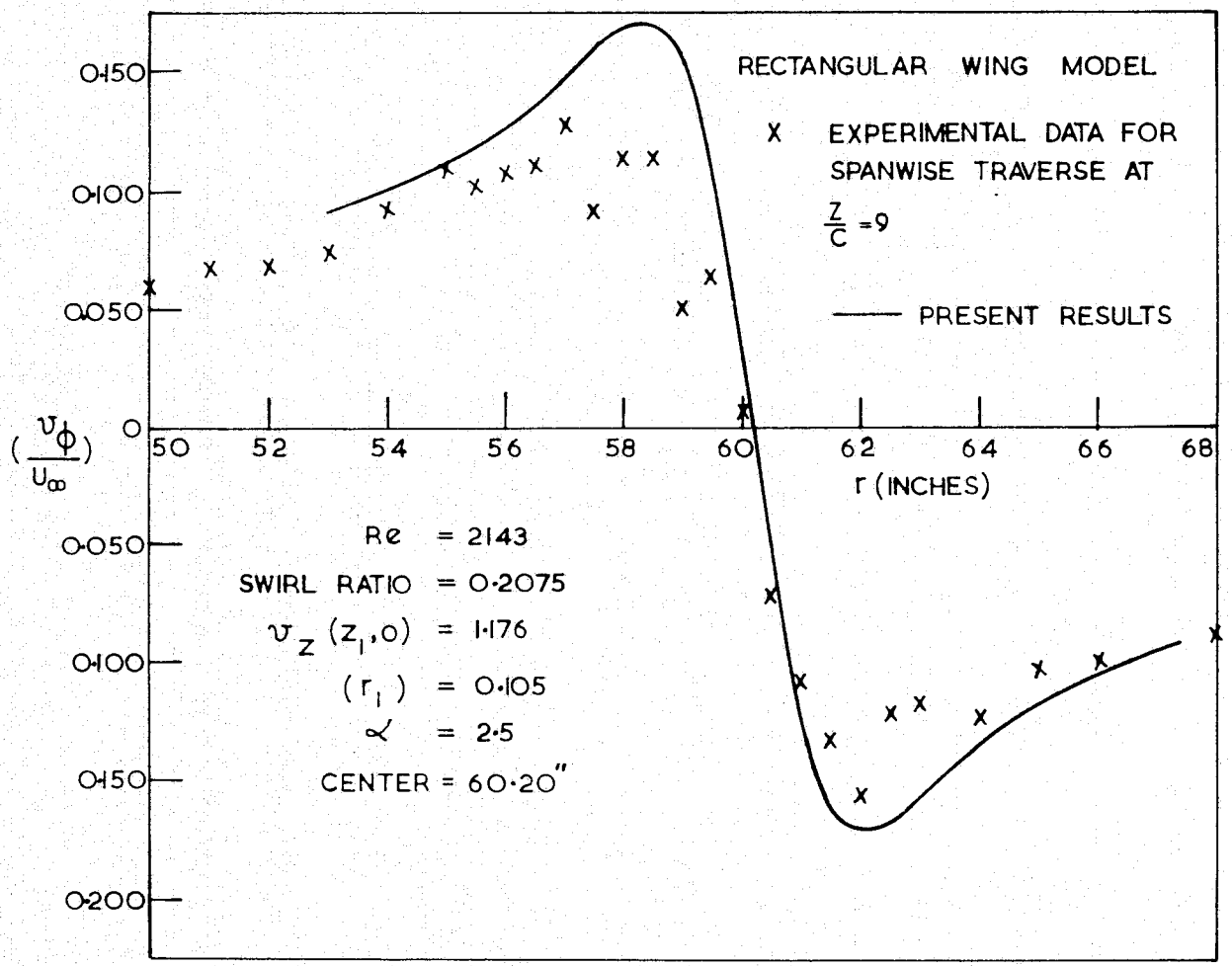

Figure 20. Comparison of the present results for (v_ϕ / U_∞) versus r with the experimental data of Reference 12.

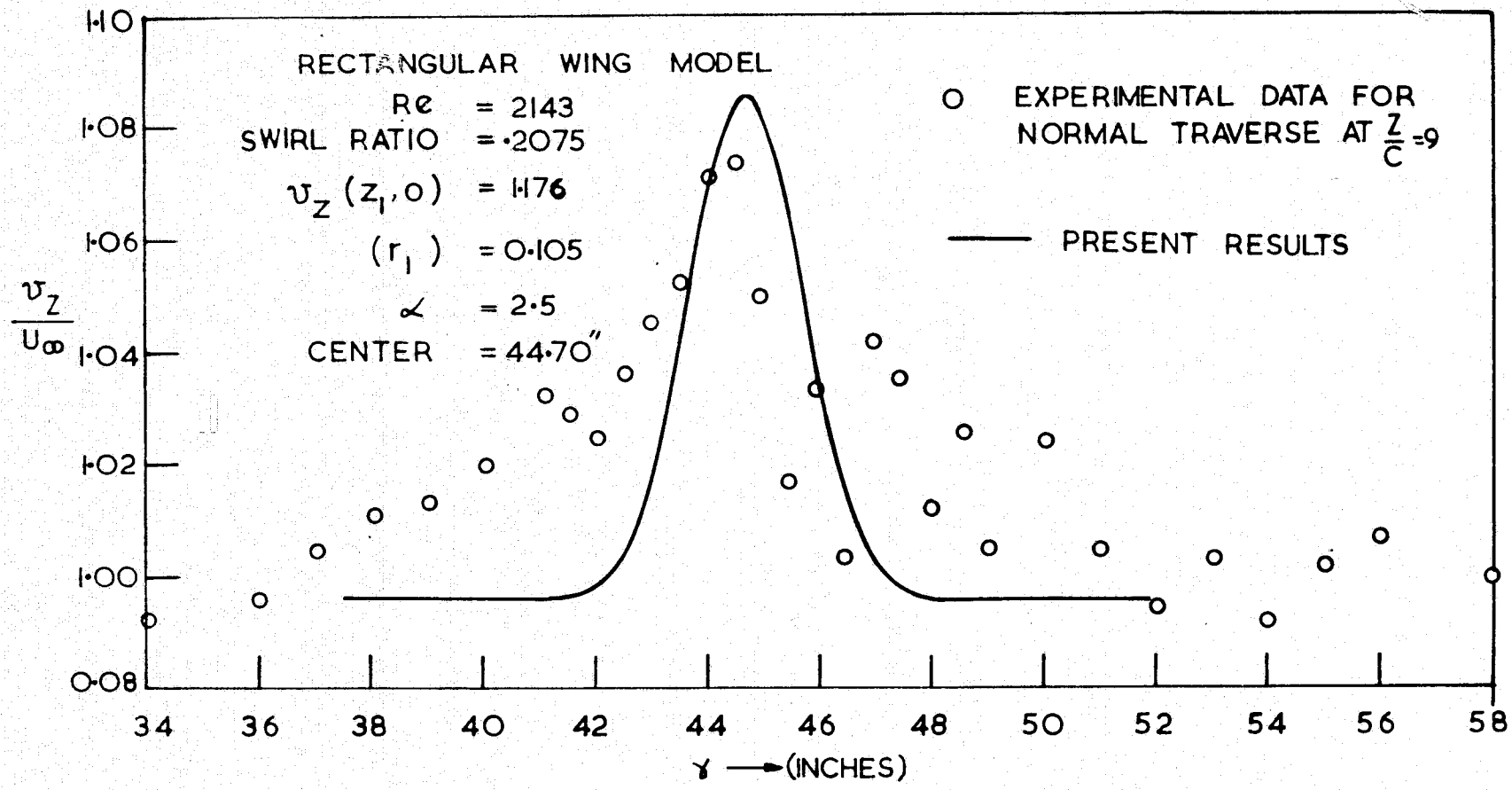

Figure 21. Comparison of the present results for (v_Z/U_∞) versus 'r' with the experimental data of Reference 12.

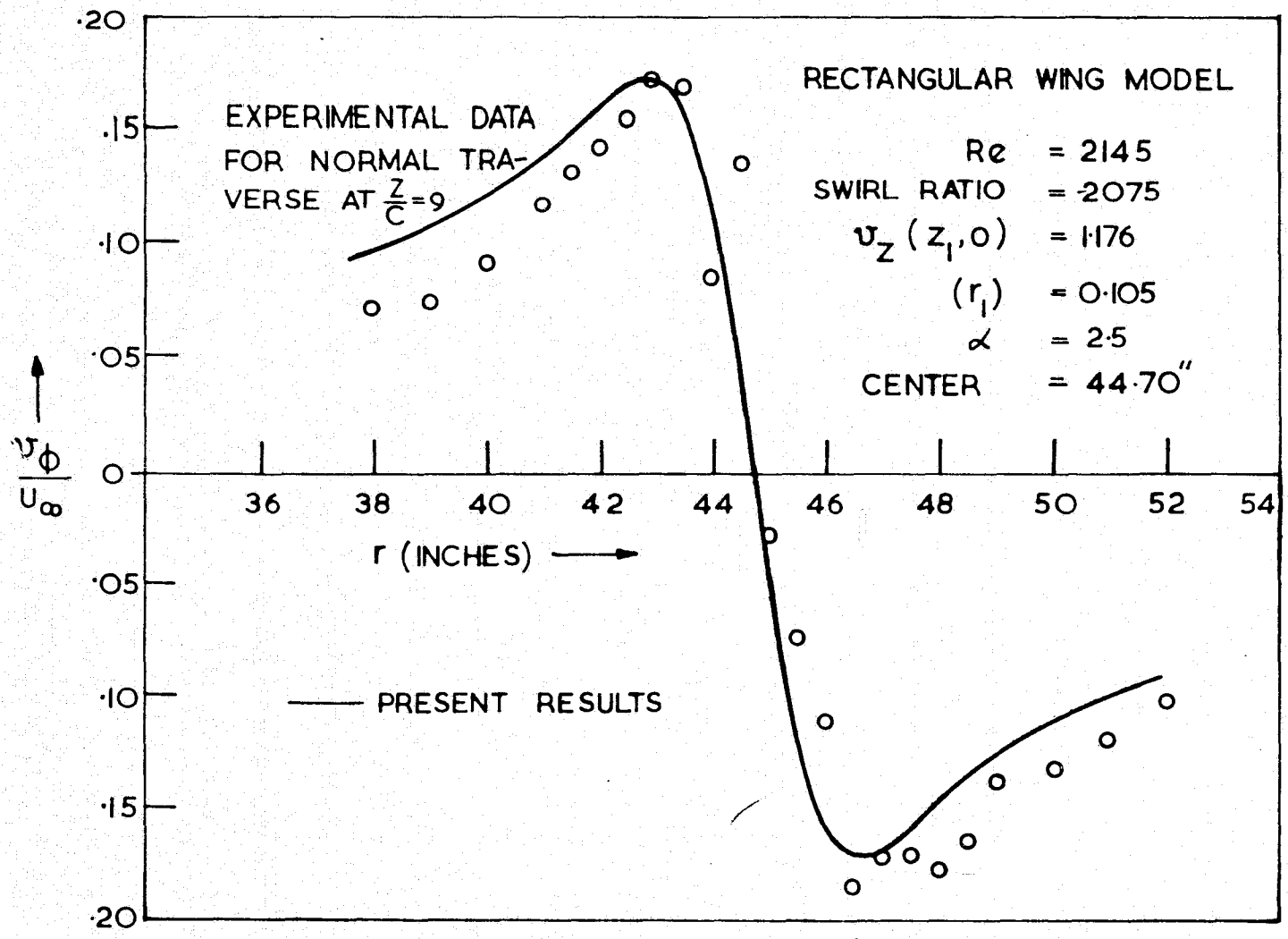

Figure 22. Comparison of the present results for v_ϕ / U_∞ versus r with the experimental data of Reference 12.

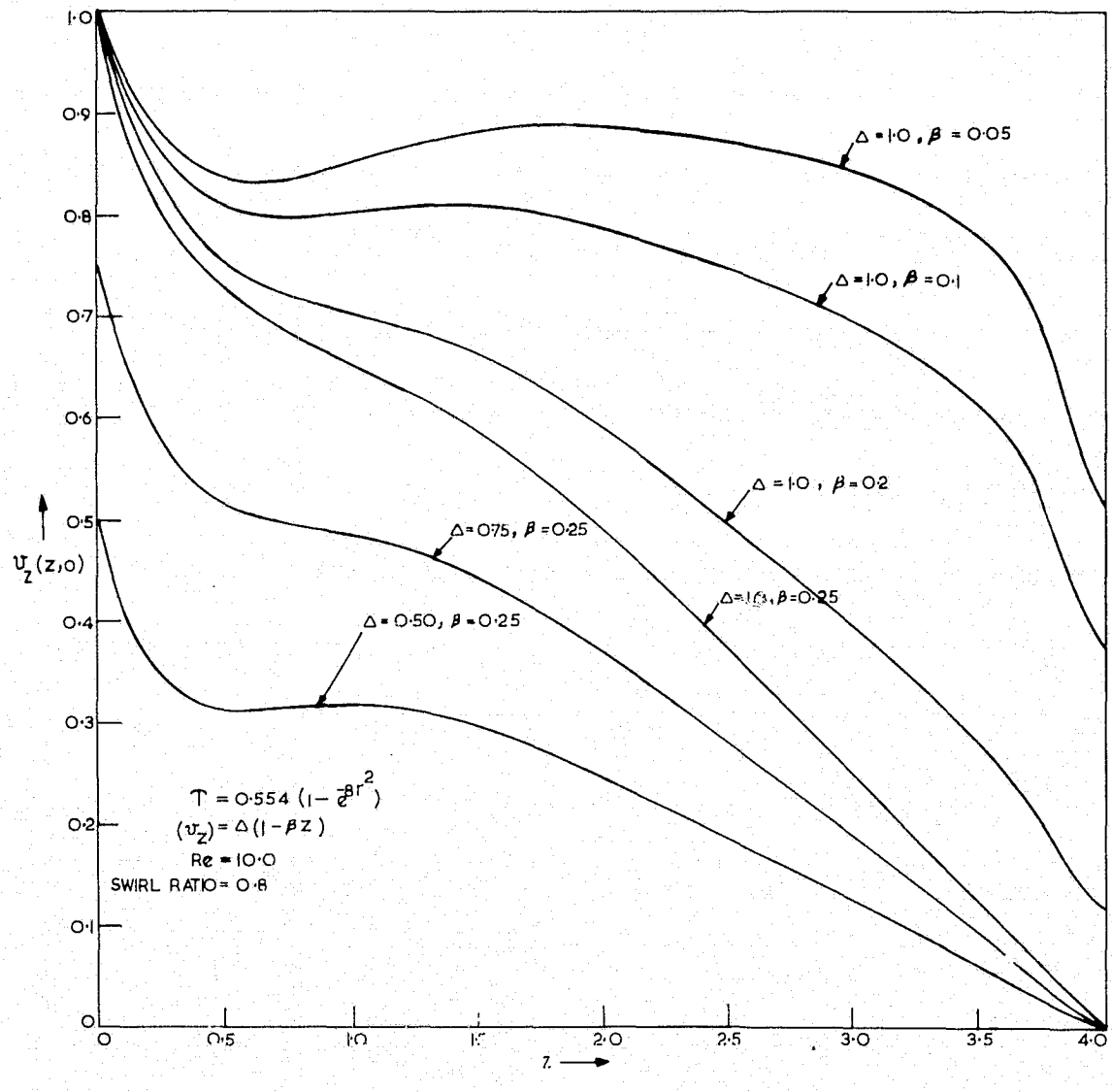

Figure 23. $v_Z(Z, 0)$ versus Z for different prescribed axial velocity at the inflow section and at the outer edge of the trailing vortex.

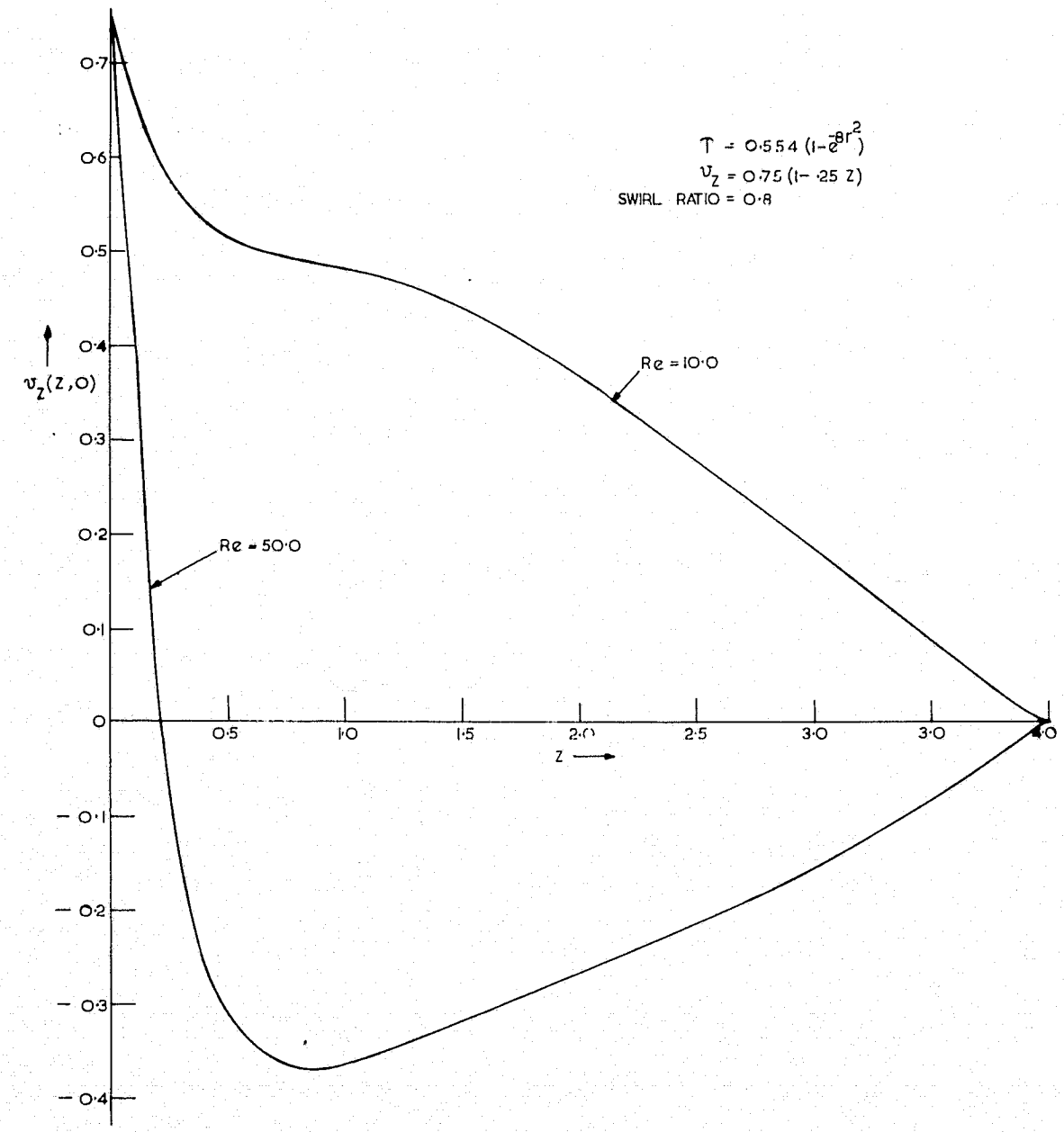

Figure 24. $v_Z(Z, 0)$ versus Z for different values of Reynolds number.

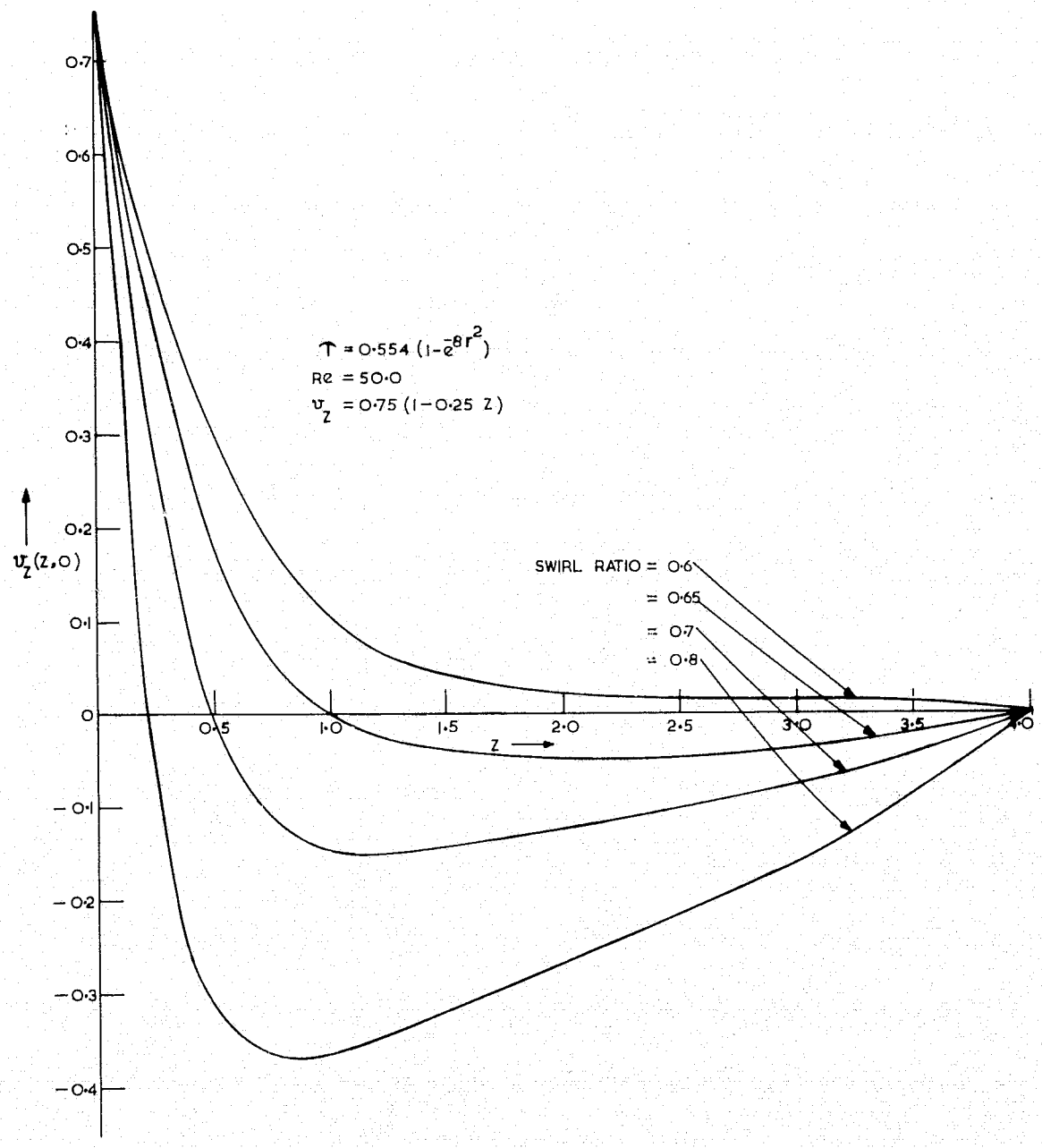

Figure 25. $v_Z(Z, 0)$ versus Z for different values of the swirl ratio.

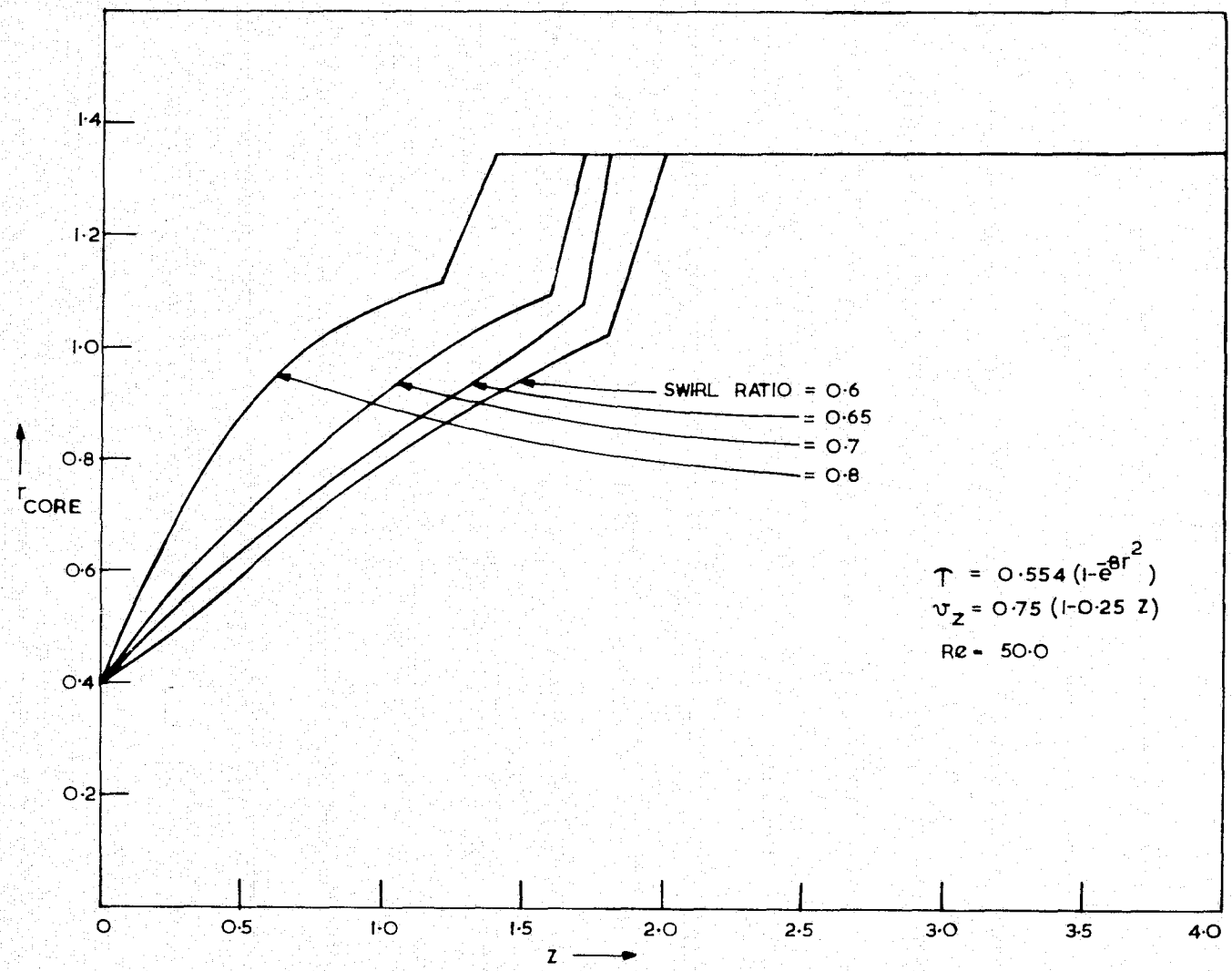

Figure 26. r_{core} versus Z for different values of swirl ratio.

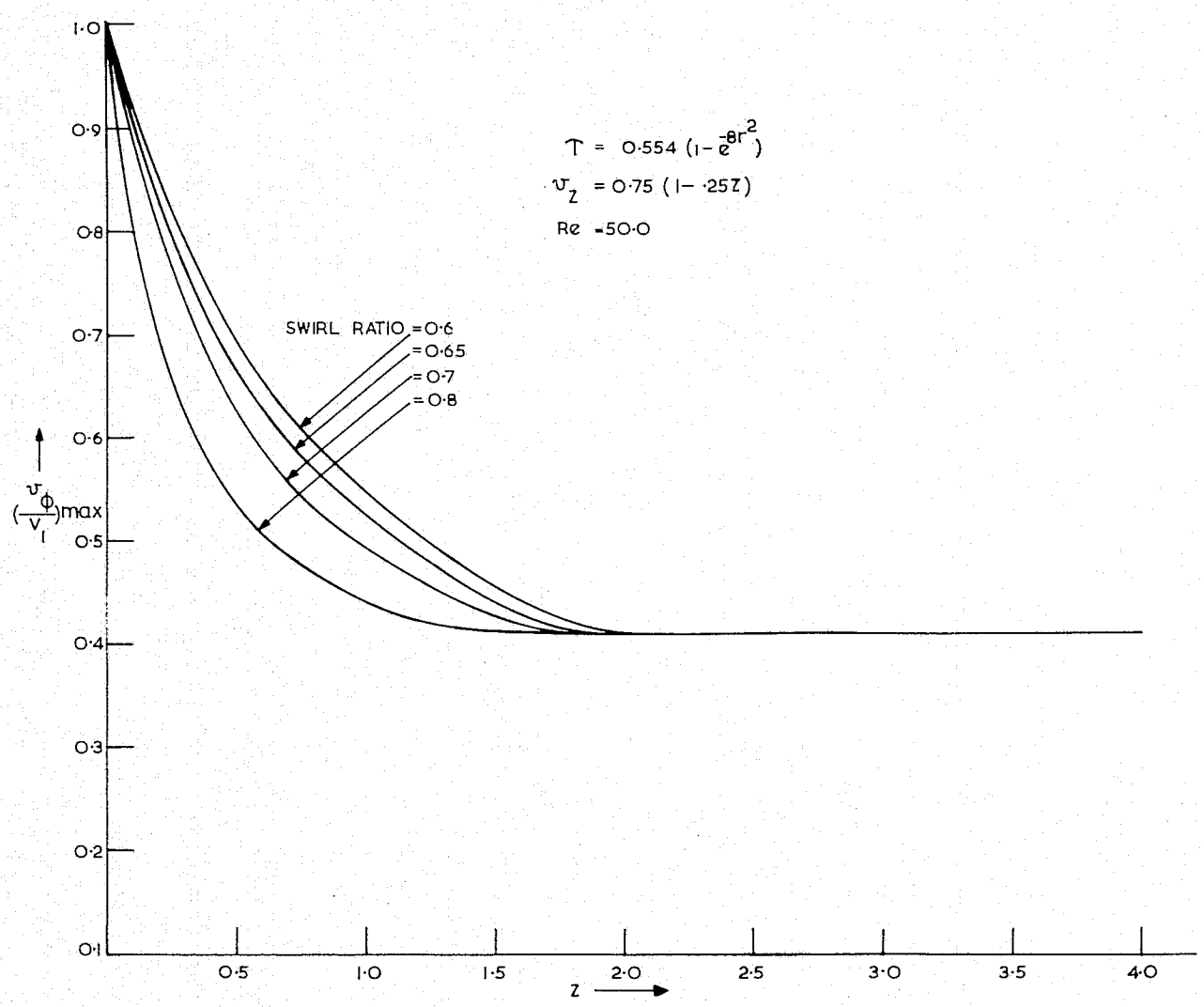

Figure 27. $(v_\phi / V_1)_{max}$ versus Z for different values of swirl ratio.

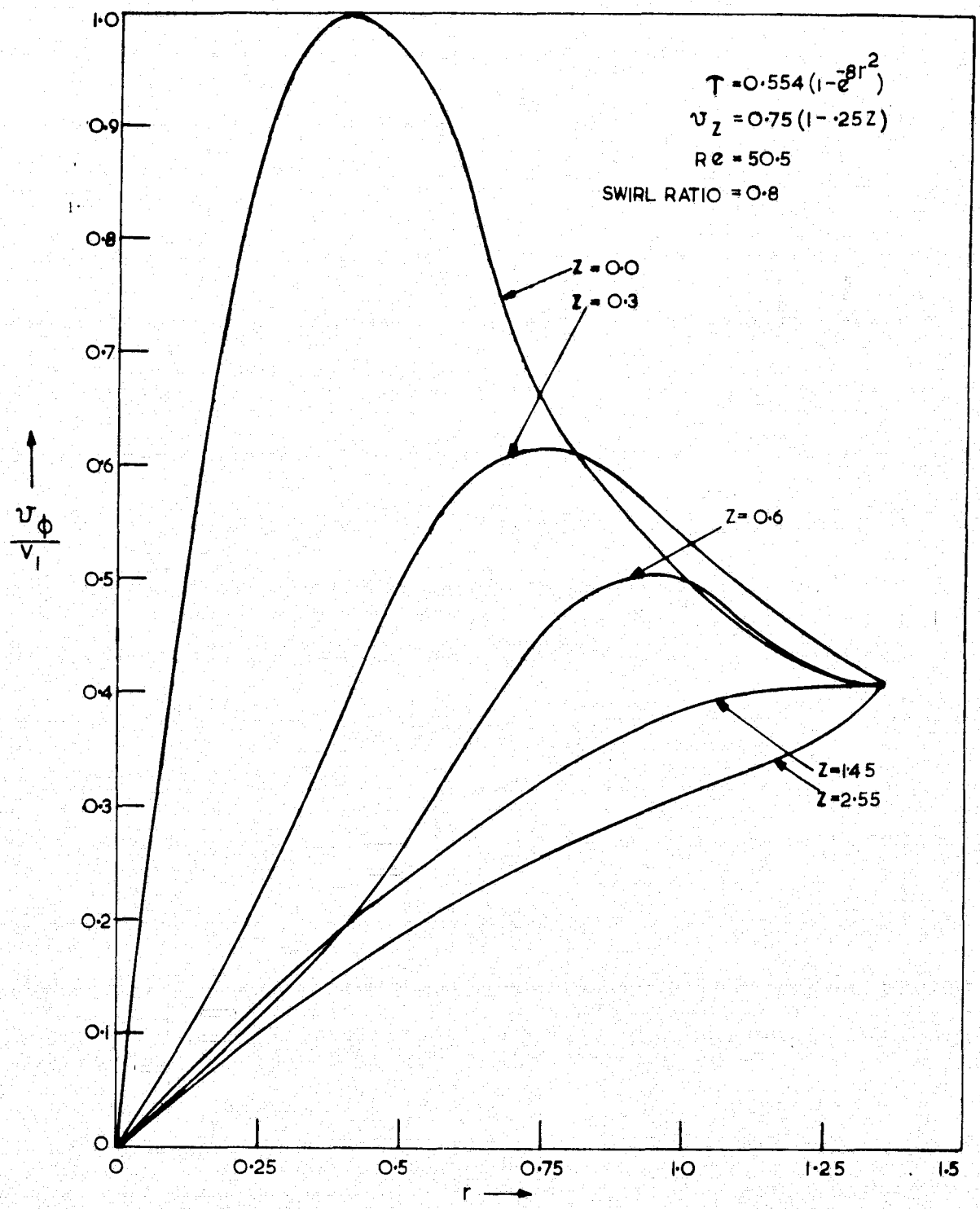

Figure 28. v_ϕ / V_1 versus r at different sections in the downstream direction.

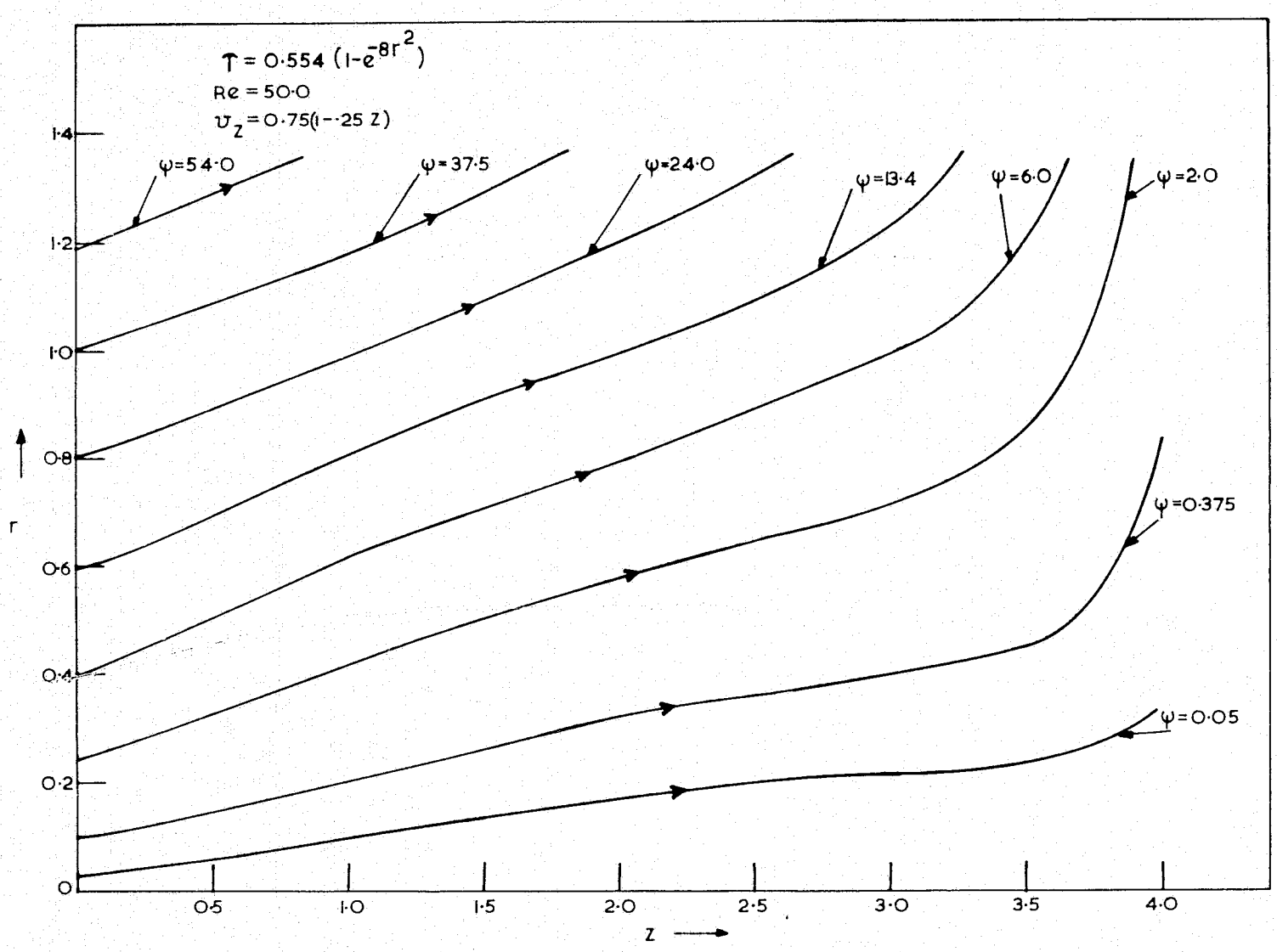

Figure 29. Streamline pattern for swirl ratio = 0.6, stream function values those shown $\times 10^{-2}$.

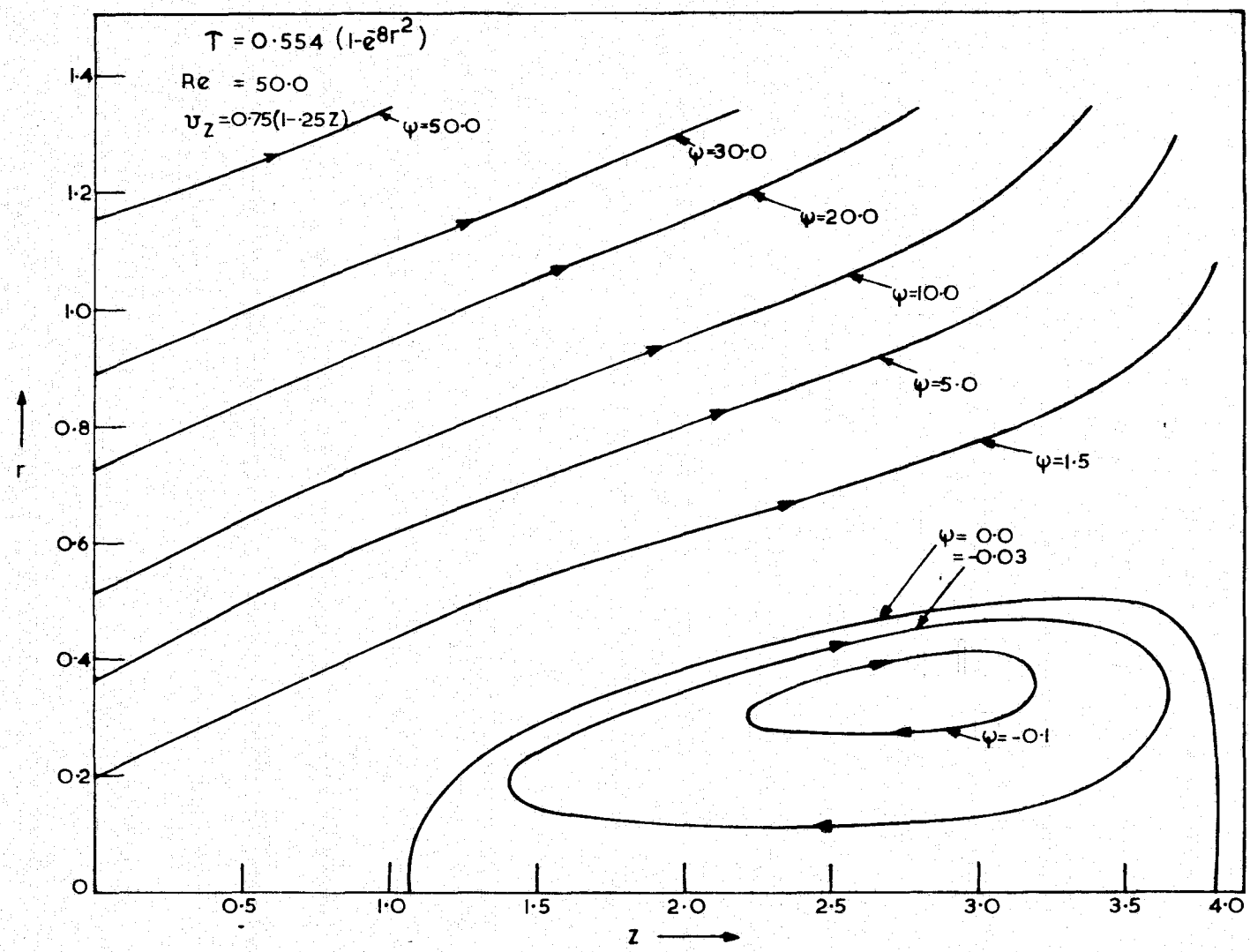

Figure 30. Streamline pattern for swirl ratio = 0.65, stream function values those shown $\times 10^{-2}$.

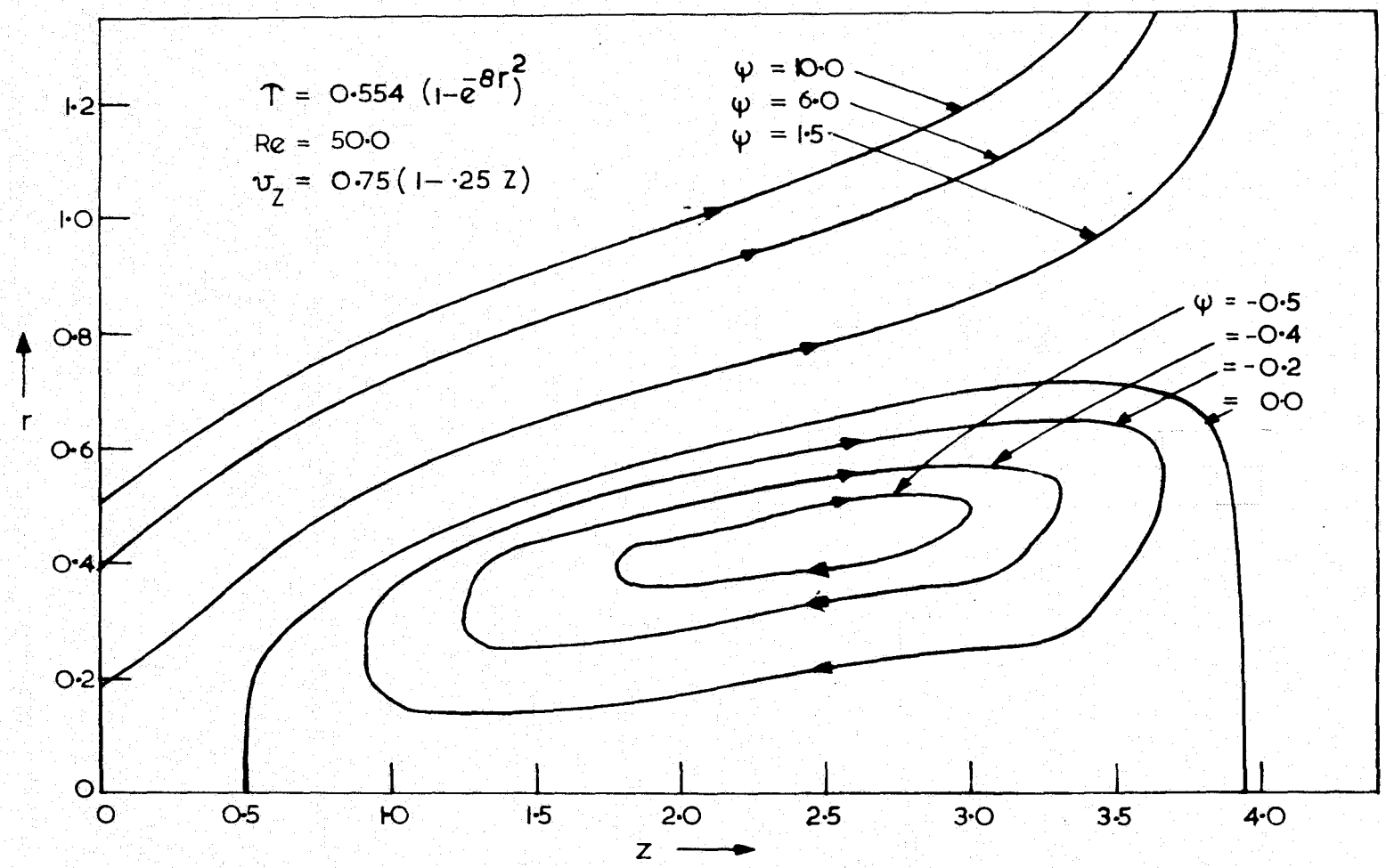

Figure 31. Streamline pattern for swirl ratio = 0.7, stream function values those shown $\times 10^{-2}$.

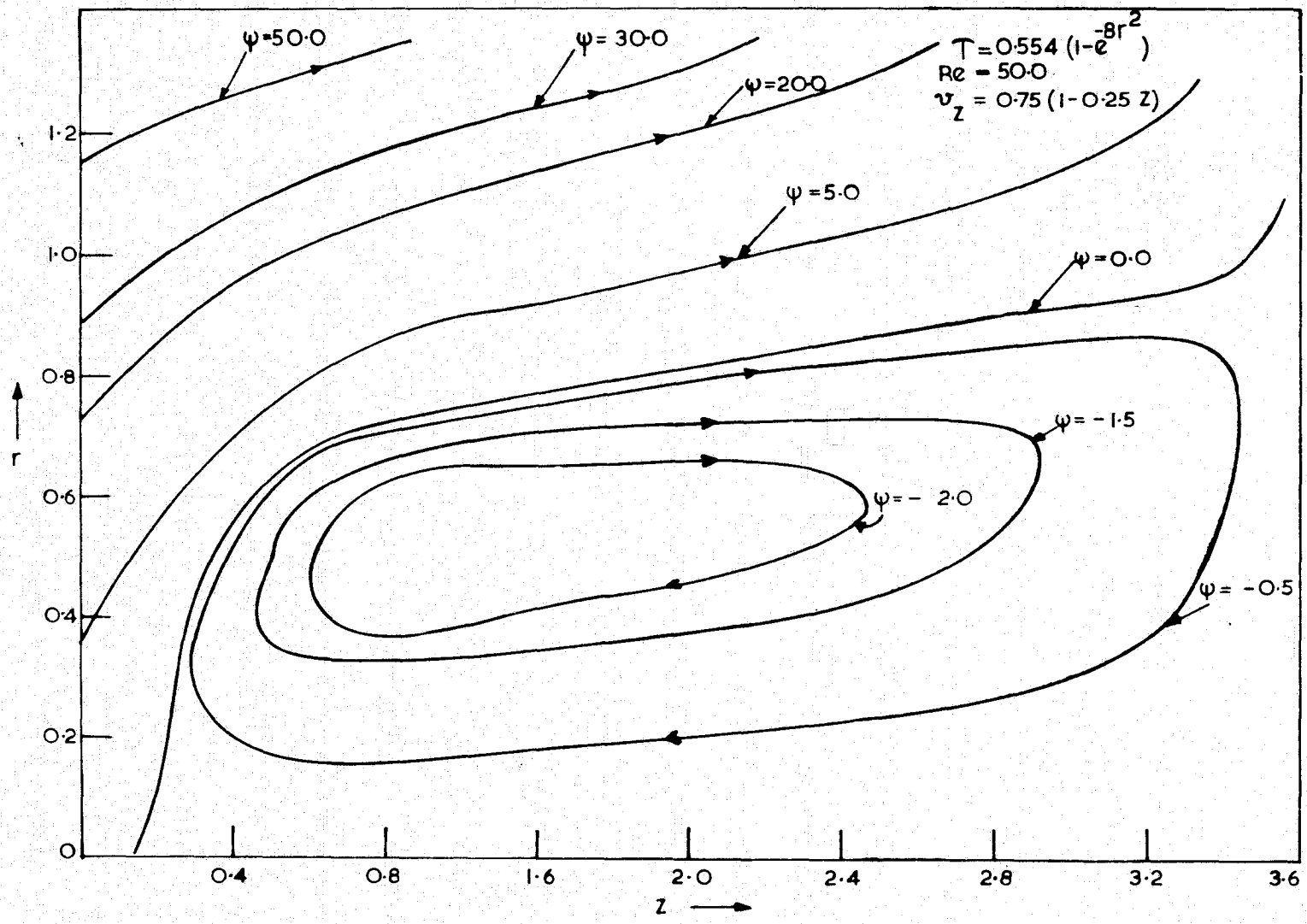

Figure 32. Streamline pattern for swirl ratio = 0.8, stream function values those shown $\times 10^{-2}$.

REFERENCES

1. Newman, B. G.: Flow in a Viscous Trailing Vortex. Aero. Quart., vol. 10, 1959, p. 149.

2. Hall, M. G.: A Numerical Method for Solving the Equations for a Vortex Breakdown. RAE TR 65106, Royal Aircraft Establishment, Farnborough, U.K., 1965.

3. Hall, M. G.: A New Approach to Vortex Breakdown. Proc. Heat Transfer and Fluid Mech. Inst., Stanford University Press, Stanford, California, 1967, p. 319.

4. Kopecky, R. M. and Torrance, K. E.: Initiation and Structure of Axisymmetric Eddies in a Rotating Stream. To appear in Int. J. Computers and Fluids (also see NASA CR-1865), Aug. 1971.

5. Bossel, H. H.: Vortex Equations: Singularities, Numerical Solutions, and Axisymmetric Vortex Breakdown. NASA CR-2090, July 1972.

6. Batchelor, G. K.: Axial Flow in Trailing Line Vortices. J. Fluid Mech., vol. 20, no. 4, 1964, p. 645.

7. Mager, A.: Dissipation and Breakdown of a Wing-Tip Vortex. J. Fluid Mech., vol. 55, part 4, 1972, p. 609.

8. Sarpkaya, T.: Effect of Adverse Pressure Gradient on Vortex Breakdown. AIAA Journal, vol. 12, no. 5, 1974, p. 602.

9. Kuhn, G. D. and Nielson, J. N.: Analytical Studies of Aircraft Trailing Vortices. AIAA Paper no. 72-42, presented at AIAA 10th Aerospace Sciences Meeting, Dan Diego, California, Jan. 17-19, 1972.

10. Hoffman, E. R. and Joubert, P. N.: Turbulent Line Vortices. J. Fluid Mech., vol. 16, part 3, 1963, p. 395.

11. Marshall, J. R. and Marchman, J. F. III: Vortex Age as a Wake Turbulence Scaling Parameter. NASA CR-132312, Aug. 1973 (also see AIAA Paper no. 74-36, 1974).

REFERENCES (Concluded)

12. Chigier, N. A. and Corsiglia, V. R.: Tip Vortices-Velocity Distributions. NASA TM X-62087, Sept. 1971.

13. Chigier, N. A. and Corsiglia, V. R.: Wind-Tunnel Test Data for Wing Trailing Vortex Flow Survey. NASA TM X-62148, May 1972.

14. Rorke, J. B. and Moffitt, R. C.: Wind-Tunnel Simulation of Full Scale Vortices. NASA CR-2180, March 1973.

15. Roache, P. J.: Computational Fluid Mechanics. Hermosa Publishers, 1972.

16. Torrance, K. E.: Comparisons of Finite Difference Computations of Natural Convection. J. Res. of the N.B.S. — B. Mathr. Sciences, vol. 728, no. 4, 1968, p. 281.

17. Fromm, J.: The Time Dependent Flow of an Incompressible Viscous Fluid. Methods in Computational Physics, vol. 3, New York, Academic Press, 1964.

18. Donovan, L. F.: A Numerical Solution of Unsteady Flow in a Two-Dimensional Square Cavity. AIAA Journal, vol. 8, no. 3, 1970, p. 524.

19. Roache, P. J. and Mueller, T. J.: Numerical Solutions of Laminar Separated Flows. AIAA, vol. 8, no. 3, 1970, p. 530.

20. Benjamin, T. B.: Theory of the Vortex Breakdown Phenomenon. J. Fluid Mech., vol. 14, 1962, p. 593.

21. Ludwieg, H.: Erklärung des Wirblaufplatzens mit Hilfe der Stabilitätstheorie für Strömungen mit schraubenförmigen Stromlinien. Z. Flugwiss., vol. 13, 1965, p. 437.

APPROVAL

NUMERICAL SOLUTIONS OF NAVIER-STOKES EQUATIONS FOR THE STRUCTURE OF A TRAILING VORTEX

By A. C. Jain

The information in this report has been reviewed for security classification. Review of any information concerning Department of Defense or Atomic Energy Commission programs has been made by the MSFC Security Classification Officer. This report, in its entirety, has been determined to be unclassified.

This document has also been reviewed and approved for technical accuracy.

J. A. LOVINGOOD
Director, Systems Dynamics Laboratory

☆U.S. GOVERNMENT PRINTING OFFICE 1977–740-049/135 REGION NO. 4